Geomorphology 452 (2024) 109122

Contents lists available at ScienceDirect

Geomorphology

journal homepage: www.journals.elsevier.com/geomorphology

Evaluating historical, basin-wide landslide activity in a context of land abandonment and climate change: Effects of landslide visibility and temporal resolution

Sharon Pittau [a,1], Mauro Rossi [b], Manel Llena [c], Francesco Brardinoni [a,*]

[a] Department of Biological, Geological and Environmental Sciences, University of Bologna, Bologna, Italy
[b] Consiglio Nazionale delle Ricerche, Istituto di Ricerca per la Protezione Idrogeologica, Perugia, Italy
[c] Pyrenean Institute of Ecology, Spanish National Research Council, Zaragoza, Spain

ARTICLE INFO

Keywords:
Landslides
Landslide visibility
Multi-temporal inventory
Temporal resolution
Badlands
Land cover change
Climate change

ABSTRACT

Drainage basins of the Northern Apennines, particularly in the clayey settings, bear among the highest rates of landsliding worldwide. A history of major land cover changes has left a landscape characterized by sparse, coppice-managed forest, transitional shrubs, and actively eroding badlands. Historical trends of landslide occurrence are examined in the Sillaro River basin (139 km^2) in relation to land cover and climatic changes. To this purpose we have compiled a multi-temporal (1954–2018) landslide inventory (n = 1164) across twelve sequential photo sets that bears decadal (7- to 15-yr) and finer (2- to 6-yr) temporal resolution respectively before and after 1996. To account for changes in meteorological forcing, we examine: (i) the total annual precipitation (PRCPTOT); (ii) the annual maximum daily precipitation (RX1day); and (iii) the precipitation fraction (R99pTOT) due to extremely wet days. We find that landslide activity is strongly controlled by lithology, with landslide densities in claystones 3-to-4 times higher than in marl-sandstone alternations. This difference is chiefly associated with badlands, which are the most active land cover type and where new scars at a site could recur up to nine times. To evaluate the influence of varying temporal resolution on inventory completeness, hence on inference about land cover and climatic effects, we constrain the time scales of landslide visibility and assess the relative rates of undersampling. We find that visibility functions decline non-linearly with time, and that an inventory compiled at 5-year resolution would be missing up to 20 % of the landslide scars, with the size of an additional 27 % that would be underestimated due to revegetation. Overall, detection of entire landslide scars, which varies with land cover, becomes rare after 13 years in transitional shrubs, and after 17 years in badlands and managed forest. The historical analysis shows that landslide count: (i) increases in 1955–1976, a period of maximum anthropogenic pressure and wetter conditions; (ii) decreases steadily from 1977 through 2000, during a phase of land abandonment and decline in annual precipitation; and (iii) grows highest in 2000–2014, a period of land cover stability characterized by lesser precipitation although increasingly focused on high-magnitude events. To evaluate the likely reason of this recent increase in landsliding (i.e., R99pTOT vs inventorying resolution), we replicate the post-1996 mapping at coarser resolution. In the simplified inventory, landslide densities drop up to a factor of 2, and the inverse correlation originally linking landslide count with R99pTOT, loses significance. We conclude that, when the bias associated with varying inventorying resolution is removed, dependencies previously attributed to climatic effects become drastically reduced, and in some instances can even disappear.

* Corresponding author.
E-mail address: francesco.brardinoni@unibo.it (F. Brardinoni).
[1] Present address: Interdepartmental Research and Innovation Centre on Construction and Environmental services, University of Modena and Reggio Emilia, Modena, Italy.

https://doi.org/10.1016/j.geomorph.2024.109122
Received 11 June 2023; Received in revised form 26 February 2024; Accepted 27 February 2024
Available online 28 February 2024

1. Introduction

Understanding the interactions between hydro-meteorological forcing and land cover dynamics is fundamental for evaluating landscape sensitivity to change and relevant geomorphic responses (Brunsden, 1993). This question is particularly critical for landscapes of the Anthropocene, where (inherited and ongoing) anthropogenic disturbance represents the main driver of landscape evolution (Llena et al., 2024), in a context of climate change (Slaymaker et al., 2009).

In the last three decades, hilly-to-mountain settings have witnessed growing interest for an improved understanding of the controls exerted by climate and land cover changes on land vulnerability and sediment fluxes (e.g., García-Ruiz et al., 1996; Piccarreta et al., 2006; Buendia et al., 2015; Zeng et al., 2018; McEachran et al., 2020; Seixas and Veldhuisen, 2023). Across the Mediterranean, these studies have observed a decrease in runoff during the second half of the 20th century, which has been interpreted as the combined effect of forest regeneration following rural abandonment and increasingly drier climatic conditions. A similar trend agrees with the historical phase of generalized channel narrowing observed in fluvial corridors between the 1950s and 1990s, which has been attributed to land-use changes on floodplains and reduced sediment supply from mountain tributaries due to hillslope afforestation (e.g., Liébault and Piégay, 2002; Scorpio and Piégay, 2021).

On the hillslopes, owing to the complexity of deciphering land-cover effects in areas with a long history of anthropogenic disturbance (Glade, 2003), the limited number of basin-wide studies and their somewhat ambiguous results, it is less clear how landslide activity has responded to such historical environmental changes. Existing studies conducted in mountain settings that require drainage maintenance (i.e., agricultural terraces and/or dense network of forest roads) have indicated that following land abandonment landslide activity tends to cluster in naturally revegetated terrain (e.g., Crosta and Frattini, 2003; Cevasco et al., 2014; Persichillo et al., 2017). Elsewhere, a more composite picture has been described (e.g., Beguería, 2006). On one hand, former arable fields on steep valley sides appeared to foster landsliding well after shrubs and forest cover re-establishment. On the other hand, stabilizing effects of natural revegetation in older forest stands and subalpine pastures were also noted. Overall, the actual rates of landsliding, and the time scales associated with highest instability and recovery in (Sidle and Ochiai, 2006; Imaizumi et al., 2008; Sidle and Bogaard, 2016) remain poorly constrained in drainage basins across the Mediterranean. This is a critical shortcoming for a basic understanding of how these geomorphic systems function, as well as for implementing suitable management strategies.

Besides experimental confounding exerted by varying agricultural practices (e.g., Persichillo et al., 2017), the observed ambiguity in landslide response may have to do with the coarse temporal resolution of the inventories utilized – sequential photos are 20 to 30 years apart (e.g., Beguería, 2006; Pisano et al., 2017) – and therefore with their degree of completeness. Decadal resolution limits landslide detection under a regenerating forest canopy (e.g., Brardinoni et al., 2003b; Turner et al., 2010), considering that landslide scars may become increasingly hidden (e.g., Smith et al., 1986; Brardinoni, 2001; Chou et al., 2009; Buma and Pawlik, 2021; Saito et al., 2022). In addition, it may lead to further undersampling, due to the overprinting (or coalescence) of landslides occurred in different years within the decade(s) bound by two sequential photos.

The foregoing sources of bias in landslide detection and mapping are likely to play a major role in highly erodible lithologies such as claystones, where badlands represent characteristic, highly dynamic features across the Mediterranean (Yair et al., 1980; Gallart et al., 2002; Nadal-Romero et al., 2021)., and landsliding at a site can recur almost annually (e.g., Pittau et al., 2021). In these settings, which host gentle, easily accessible hillslopes, major forest clearing began in the Roman Period and continued throughout the 20th century, likely promoting widespread erosion and badland development (e.g., Torri et al., 2018).

While badland dynamics associated with surficial erosion has been the focus of extensive investigations (e.g., Benito et al., 1992; Regüés et al., 1995; Mathys et al., 2003; Nadal-Romero et al., 2012; Torri et al., 2013; Vergari et al., 2013; Vericat et al., 2014; Aucelli et al., 2016; Ranga et al., 2016; Bosino et al., 2019; Llena et al., 2020), the role of landsliding has received much less, mostly qualitative, attention (e.g., Della Seta et al., 2009; Vergari et al., 2019; La Licata et al., 2023). This gap, together with the limited number of basin-wide studies, and the lack of information on the uncertainty associated with landslide inventorying across sequential photosets, have prevented systematic evaluation of how land cover changes may affect landslide occurrence in weak lithologies, such those of the Northern Apennines, in relation to ongoing climatic changes.

To start addressing this set of interrelated gaps, we selected the mountain portion of the Sillaro River, a clay-dominated basin in the Northern Apennines, where badlands are common and slope failures chiefly occur as earth slides and earthflows (Pittau et al., 2021). Here, societal changes associated with post-Second World War recovery and modern industrial development, led to major displacement of rural communities to cities and thus to land abandonment, with consequent regeneration of transitional shrubs and natural forests (Preciso et al., 2012; Pavanelli et al., 2019).

In the Sillaro basin, this work aims to: (i) evaluate the strength of possible lithologic effects on historical landslide occurrence; (ii) constrain the time window associated with landslide visibility on aerial photos across land cover types; and finally (iii) explain historical trends of landslide occurrence in relation to concurrent land cover and climatic changes, with explicit reference to the geomorphic significance of badlands. To these ends, we have manually compiled a multi-temporal landslide inventory (1954–2018) across twelve sets of optical imagery. Coherently with increasingly available high-resolution optical imagery, our historical inventory may be split into an older part, characterized by coarse decadal resolution (between 1954 and 2000), and a more recent one in which sequential photos are 2 to 3 years apart (Table 1). Such a composite multi-temporal setup lends opportunity to test how our evaluations on land cover and climatic effects may depend on the temporal resolution of the inventory. To pursue this additional objective, we conclude our work by replicating the post-1996 inventorying procedure

Table 1
Historical aerial photographs and orthophoto mosaics used for multi-temporal landslide identification and mapping.

Photo year	Month of acquisition	Nominal scale	Pixel size (m)	Bands	Source
1954	Jul	1:55,000	1[a]	BW	IGM
1969	Jun-Sept	1:15,000	0.7[a]	BW	E-R Region
1976	Apr-Jul	1:13,000	0.9[a]	RGB	E-R Region
1985–88	Apr-Jul	1:25,000	1	BW	E-R Region
1996	Sept	1:10,000	1	BW	E-R Region
2000	Jun-Jul	1:10,000	1	RGB	WMS GN[b]
2006	Apr-Jul	1:10,000	0.5	RGB	WMS GN[b]
2008	Jun-Aug	1:10,000	0.5	RGB	WMS E-R[c]
2011	May-Jun	1:10,000	0.5	RGB	WMS E-R[c]
2014	May-Sept	1:10,000	0.5	RGB	E-R Region
2016	Sept	1:10,000	0.3	RGB	Google Earth
2018	May-Sept	1:10,000	0.3	RGB	WMS E-R[c]
2020	Apr-Aug	1:10,000	0.2	RGB	WMS E-R[c, d]
2022	Sept	1:10,000	0.3	RGB	Google Earth[d]

[a] Available also as paper stereo pairs.
[b] Geoportale Nazionale: http://www.pcn.minambiente.it/mattm/servizio-wms/
[c] Geoportale Regione Emilia-Romagna: https://geoportale.regione.emilia-romagna.it/servizi/servizi-ogc/elenco-capabilities-dei-servizi-wms
[d] Used for the multi-temporal visibility test only.

at coarser (i.e., decadal) resolution and discuss relevant implications.

2. Study area

The study area includes the mountain portion of the Sillaro River basin (139 km^2) located in the Bologna Metropolitan Area, Italy (Fig. 1a). Elevations range from 56 m a.s.l. in Castel San Pietro Terme, at the basin outlet, to 993 m, at Mt. La Fine, on the main divide of the Northern Apennines. The Sillaro River flows along a key regional geologic transition, where the Ligurian Unit (Cretaceous-Eocene) and the Umbro-Marchean-Romagna succession (Miocene-Pleistocene) come into contact, in proximity of the basin's south-eastern end (Zattin et al., 2002; Benini et al., 2009; Bettelli et al., 2012). Accordingly, the area encloses four main geologic domains, in which clayey lithologies prevail (Fig. 1b). Claystones and lesser sandy, poorly cemented arenites of the Padano-Adriatic domain (Upper Messinian-Pleistocene; hereafter termed Padano-Adriatic claystones) make up 22 % of the area in the lower portion of the basin (Figs. 1b and 2b). Alternations of claystones and lesser marls, and poorly cemented arenites of the Epiligurian domain (Eocene-Miocene; hereafter termed Epiligurian claystones), mainly outcrop in the central part of the basin (24 % of basin area). Alternations of claystones and lesser marls of the Ligurian domain (Cretaceous-Eocene; hereafter termed Ligurian claystones), outcrop chiefly in the middle and upper part of the basin (36 % of basin area; Figs. 1b and 2b). Ligurian claystones incorporate highly tectonized limestone blocks and exhibit chaotic texture. Finally, sandstones and marls of the Umbro-Marchean flysch complex (Serravallian-Tortonian; hereafter termed Sandstones and Marls) cover the remainder 10 % of the area, in the upper south-eastern portion of the basin (Figs. 1b and 2b).

The hillslopes and the ephemeral gully network carved on clay-bearing lithologies host widespread badland systems (i.e., the so-called *calanchi* in Italian). Dominant landslide types are earth slides and earthflows (Bertolini and Pizziolo, 2008; Simoni et al., 2013; Pittau et al., 2021). These geomorphic processes produce and deliver sediment to major alluvial fans at tributary confluences and to the main Sillaro River floodplain, which collectively occupy 8 % of the basin area. The Sillaro River has a complex channel pattern. It starts as a single-thread, semi-confined channel, characterized by riffle-pool and plane-bed morphology, nested in a plateau-like upper valley segment. In proximity of Sassoleone (Fig. 1a), the channel becomes substantially steeper and flows along tightly confined and strongly coupled reaches, fed by lateral earth slides and earthflows. Upstream of San Clemente (Fig. 1a), the river degrades to multi-thread unconfined and semi-confined channel reaches, along the main alluvial floodplain.

The variation of slope gradient as a function of elevation (Fig. 2a), as well as the frequency distributions of elevation (Fig. 2b) and slope gradient (Fig. 2c) across geologic domains, reflect the foregoing basin configuration. Accordingly, median slope increases directly with elevation across the area occupied by the main alluvial floodplain and the alluvial fans at major tributary confluences (i.e., <200 m a.s.l., Fig. 2a). At higher elevation, slope gradient ranges between 25 and 30 %, with a subtle inflection between 600 and 800 m a.s.l., in correspondence of the aforementioned plateau, before reaching the main summits at the orogen divide (Fig. 2a). In line with the spatial distribution of the main geologic domains (Fig. 1b), the Padano-Adriatic (P-A) claystones plot at lowest elevations (i.e., peak at about 200 m a.s.l.), Epiligurian (E) claystones sit at intermediate elevations (i.e., peak at about 350 m a.s.l.), whereas Ligurian (L) claystones, and even more so, sandstones and marls of the Umbro-Marchean domain, prevail above 500 m a.s.l. (Fig. 2b). Slope frequency distributions across lithologies are similar, and peak at values comprised between 22 % and 28 %. In this context, Ligurian and Epiligurian lithologies tend to occupy respectively

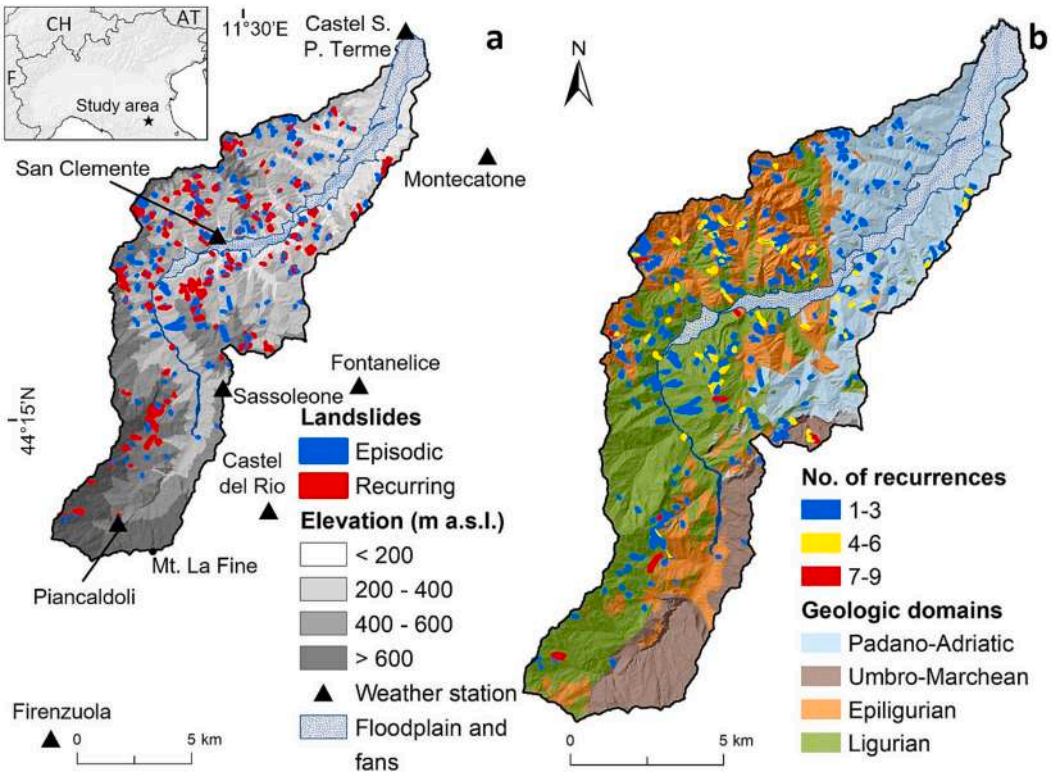

Fig. 1. Multi-temporal inventory maps (1954–2018) of the Sillaro River basin showing: (a) landslide polygons classified into episodic and recurring types on elevation bands (grey shades); and (b) landslide polygons classified by number of recorded recurrences in the context of the main geologic domains. In panel a, triangles indicate weather stations. "Floodplain and fans" in the legend of panel b indicate terrain occupied by the Sillaro River floodplain and the main alluvial fans at tributary confluences. Each landslide polygon encloses the initiation and transportation zones, and excludes the deposition zone. The inset map shows the location of the Sillaro River basin (black star).

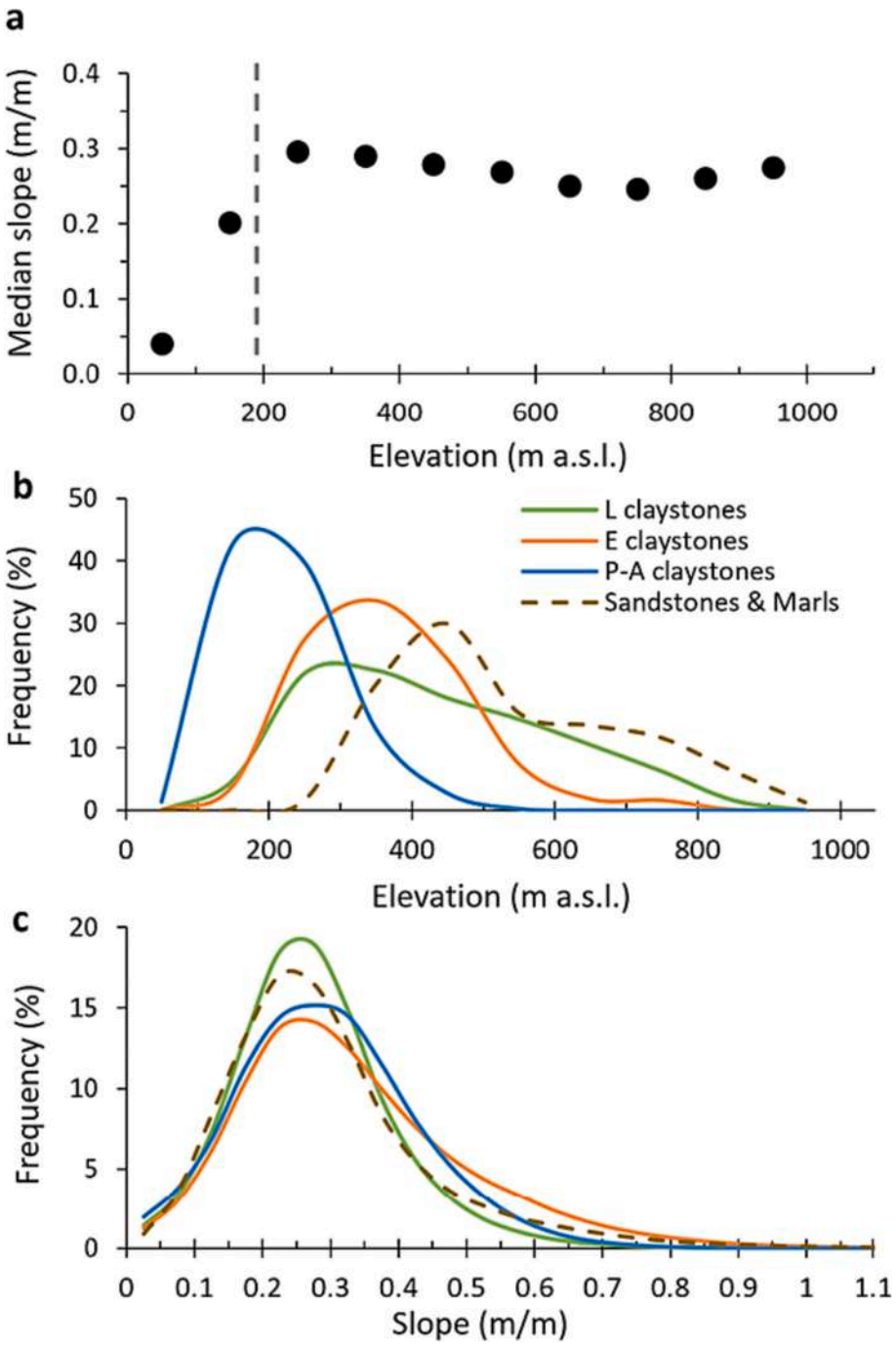

Fig. 2. (a) Median slope as a function of elevation in the Sillaro River basin; (b) altitudinal frequency distribution; and (c) slope frequency distribution across the geologic domains. Dashed line in panel a marks the approximate altitudinal limit of terrain occupied by the Sillaro River floodplain and the main alluvial fans.

the largest and smallest proportions of steep terrain (i.e., >50 %) (Fig. 2c).

According to the Köppen-Geiger climate classification, the study area belongs to the Mediterranean climatic zone, characterized by four seasons including hot, dry summers, cool, moderately dry winters and wetter springs and falls. Mean annual precipitation (1991–2019) increases with elevation, from 770 mm at Castel San Pietro Terme (59 m a.s.l.) to 1230 mm at Firenzuola (476 m a.s.l.) (Fig. A.1).

Today, land cover on the slopes includes arable crops and meadows (33 %), transitional shrubs (25 %) dominated by rush broom (*Spartium junceum*), juniper (*Juniperus communis*), and dog rose (*Rosa canina*), and coppice-managed forest (22 %), where downy oak (*Quercus pubescens*) and manna ash (*Fraxinus Ornus*) prevail. Badlands occupy about the 12 % of the basin, followed by urban areas (5 %), water bodies (2 %), and orchards (1 %).

3. Methods

The multi-temporal landslide inventory was compiled in GIS (Geographic Information System) environment. First, we identified and mapped landslide tracks through visual inspection of twelve sequential aerial photosets (i.e., stereoscopic photographs and/or digital orthoimagery taken in 1954, 1969, 1976, 1985–88, 1996, 2000, 2006, 2008, 2011, 2014, 2016 and 2018) (Table 1). Then we recorded movement type, which include rotational earth slides (slumps), earthflows and complex earth movements (Cruden and Varnes, 1996).

For each landslide polygon, we extracted a series of additional attributes, including area, photo year of first identification, temporal nature of occurrence, geological domain, and land cover at initiation (Table 2). Each landslide polygon encloses the perimeter of the total disturbed area, composed by an initiation and a transportation zone - down to the point where scouring could be identified - and by a deposition zone, where bulging was apparent. The characterization of landslide geometry presented in this paper follows the specifics adopted by Brardinoni et al. (2009). As such, landslide area refers to the initiation and transportation zones only, as opposed of considering the total disturbed area. This approach wishes to avoid confounding associated with different styles of deposition among movement types.

Given the coarser quality and resolution of aerial photos acquired in 1954 and the 1980s (Table 1), we set a minimum landslide width of about 4 m, beyond which we found it was not possible to assuredly delineate the landslide polygon outline through time. Landslides below this threshold width were not mapped in any of the photo sets. Our inventory targets landslides associated with a clear transfer of material from an initiation zone, through a transport zone and down to a deposition zone. Therefore, it does not include incremental seasonal movements, which may be detected through direct monitoring, InSAR, and/or feature tracking.

In the inventory, the photo year represents the minimum age for each landslide, the upper temporal boundary being constrained by the date of the antecedent aerial photo set. Following this logic, landslides mapped on 1954 photos lack of a definite temporal constraint. Finally, the temporal nature of landslides, that is episodic or recurring, was also recorded, including the number of recurrences at any given site. With reference to the study period, we classify as episodic those landslides that occur at sites with no recorded prior activity, and recurring those characterized by repeated activity i.e., testified by the appearance of new distinct headscarps and/or deposition lobes.

To evaluate possible linkages between landslide activity and hydro-meteorological forcing during the 1954–2018 study period, first we have looked at the historical coverage of daily and annual precipitation data. Owing to incomplete coverage at both the daily and annual scales at any of the weather stations (Fig. A.2), we have reconstructed the historical series of annual precipitation (and computed the relevant anomaly) by combining data from Piancaldoli (500 m a.s.l.) and San Clemente (166 m a.s.l.) weather stations (Fig. A.3). In this context, wishing to explore additional precipitation metrics against which evaluate landslide activity as mapped across 1954–2018 sequential photo sets (Table 1), we decided to use E-OBS meteorological data analogues, available on the Climate Data Store website (CDS, 2021).

E-OBS is a high-resolution daily gridded (0.25 degrees) land-only observational dataset over Europe generated through the interpolation of data recorded at meteorological stations. The terrain of the Sillaro River basin encompasses three of such grid cells (Fig. A.4). In this work, we have used data from the cell that occupies the central part of the basin, where the majority of the landslide clusters and where the San Clemente station is located.

Starting from gridded daily rainfall data, we derived the following climatic indices: (i) the annual total precipitation (PRCPTOT in mm), (ii) the annual maximum daily precipitation (RX1day in mm), and (iii) the precipitation fraction (%) due to extremely wet days i.e., when daily precipitation amount exceeds the 99th percentile in the 1950–2020 period (R99pTOT as percentage). These indices are typically used in climatology to explore historical precipitation trends across different datasets worldwide. More recently, they have been considered as possible proxies for evaluating hydro-meteorological correlations with the occurrence of natural hazards including floods, flash floods and mass movements (e.g., Ávila et al., 2016; Mysiak et al., 2018; Coscarelli et al., 2021). Specifically, PRCPTOT accounts jointly for the total surface runoff and infiltration in a year, potentially triggering saturation-related hillslope instabilities (e.g., landslides) and runoff-supported processes (e.g., flows and surficial erosion). R99pTOT considers only the amount of precipitation recorded during extreme events in a year, hence predominantly those producing intense surface runoff and potentially triggering runoff-supported processes of mass transfer. By contrast, RX1day accounts for the single highest daily rainfall amount recorded in a year, which during exceptional (short and intense) events may trigger diffused runoff and related geomorphic processes of mass transfer.

In the search for possible causal linkages between landslide activity and precipitation (e.g., Crozier, 2010; Zêzere et al., 2015; Ciccarese et al., 2021; Luna and Korup, 2022), the values of the climatic indices were aggregated according to the temporal spacing of the sequential photo sets. This type of aggregation ensures a coherent temporal alignment with the tallying of landslide occurrences detected and the relevant landslide areas mapped. Considering the specific nature of each index, aggregation functions within each time period included: (i) the *sum* of PRCPTOT, (ii) the *mean* of R99pTOT, and (iii) the *maximum* of RX1day (see Sections 4.5 and 5).

To assess land cover effects on landslide activity through time, we have drawn historical data in vector format from regional Webgis Data Repositories (i.e., Regione Emilia-Romagna, 2023; Regione Toscana, 2023). These cartographic data, which cover years 1853, 1954, 1976, 1994, 2003, 2008, 2011, 2014, and 2017, were checked through visual inspection of the relevant orthophoto mosaics, and mapping discrepancies identified were manually corrected. Starting from the Corine (2023)-based classification scheme (i.e., Corine level 4) we have subdivided land cover into four main categories, including: (i) arable crops and meadows (for brevity termed *arable crops*), (ii) transitional shrubland (for brevity termed *transitional*), (iii) managed forest, and (iv) badlands. Among the foregoing historical land-cover maps, the one published in 1853, which was manually digitized from the original Austrian Topographic Map (Kaiserlich-Königliches Militär-Geographisches Institut, 1851), does not distinguish badlands from the surrounding land-cover types; consequently, it will be used only as first order indication of the areal extent occupied by managed forest, transitional shrubs and arable crops.

Simplistically, based on highest root cohesion and water interception following plantation after forest harvesting (Sidle and Ochiai, 2006, and references therein), one would expect to observe lowest landslide activity in managed forest (most stable terrain), and a progressive increase in transitional shrubland, arable crops, and badlands (least stable terrain). However, natural forest regeneration in the Mediterranean following land abandonment in settings where agricultural practices required systematic structural (e.g., agricultural terraces) and drainage (e.g., road ditches and culverts) maintenance, proved ineffective at buffering slope instability (e.g., Cevasco et al., 2014; Persichillo et al., 2017). To test which conceptual hierarchical scheme may hold true in the Sillaro River basin, also in consideration that historical agricultural practices, locally, did not entail the construction of terraces or other

Table 2
Landslide attributes considered and analysed in this study (modified from Pittau et al., 2021).

Attribute	Category or units
Landslide size	Initiation and transportation zone (m^2)
Landslide type	Earthflow
	Earth slide
	Complex
Photo year of activity	From 1954 to 2018 (cf. Table 1)
Temporal nature	Episodic
	Recurring
Geologic domain (dominant lithologies)	Ligurian (L claystones)
	Epiligurian (E claystones)
	Padano-Adriatic (P-A claystones)
	Umbro Marchean (Sandstones and marls)
Land cover at initiation	Arable crops (and meadows)
	Transitional shrubland
	Managed forest
	Badlands

high-maintenance man-made structures, we will assess land cover effects on landslide activity in terms of landslide density, calculated as the number of occurrences per unit area – in a given land cover category – per unit time (i.e., #/km^2/yr).

In this context, bearing in mind that a landslide scar remains completely (or partly) visible for limited time since occurrence (e.g., Smith et al., 1986; Brardinoni, 2001; Buma and Pawlik, 2021; Saito et al., 2022), evaluation of land cover effects is tightly related to the temporal resolution of the landslide inventory i.e., the time interval that separates an aerial photoset from the next. To evaluate the extent to which this limitation applies to our inventory – especially before 1996, when temporal separation between sequential photosets ranges from 7 to 15 years – we ran a landslide visibility test in the post-2000 period, when photos are 2 to 3 years apart. In particular, we selected 68 landslides that first appeared (and/or last recurred) on photo years 2006, 2008, 2011 and 2014, and evaluate through time our ability to identify and map: (i) the entire landslide polygon outline (i.e., initiation and transport zones); (ii) a portion of it; or (iii) not at all, due to vegetation regrowth, surficial erosion, and/or fluvial reworking. This analysis is limited to managed forests, transitional shrubs, and badlands. Croplands were excluded due to the very limited number of landslides observed in post-2000 photographs, and to the possible confounding associated with

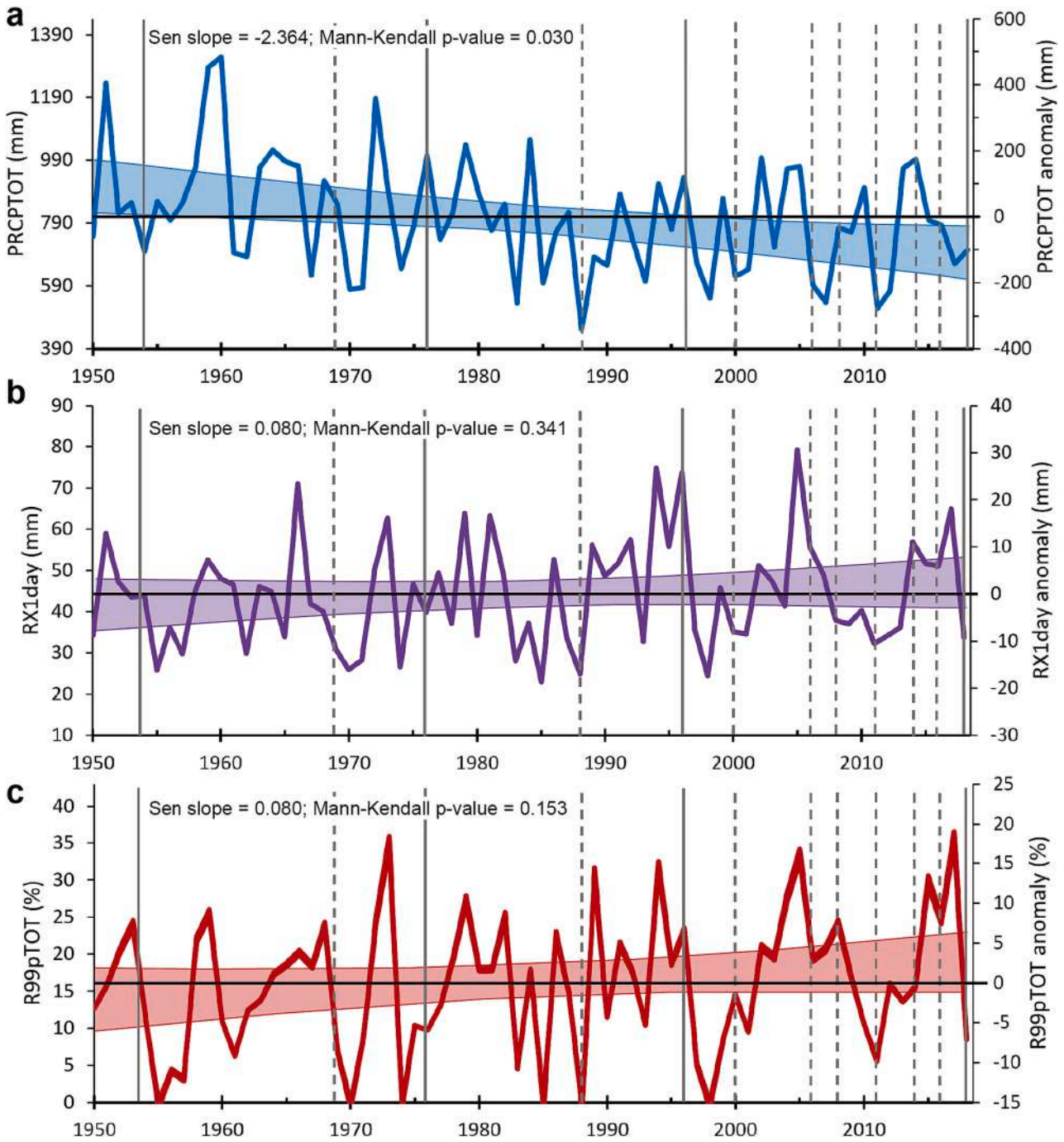

Fig. 3. Historical time series (1950–2018) of climatic index values and respective anomalies calculated from E-OBS gridded data at San Clemente station: (a) total annual precipitation (PRCPTOT); (b) RX1day; and (c) R99pTOT. Dashed vertical lines indicate the historical photo years used in the inventory. Solid vertical lines bound the time period used for assessing historical land cover effects. Despite obvious decline in PRCPTOT and increase in R99pTOT, these trends tested not significant to Mann-Kendall analysis at 0.01 level (Table A.1).

seasonal agricultural practices, which may erase/mask landslide scars.

In this paper, after characterizing the historical context of land-cover changes and concurrent variability in precipitation, we start with the examination of the landslide occurrence and recurrence across the main geologic domains. Using a subset of landslides identified on photo years comprised between 2000 and 2021, when photos are 2 to 3 years apart, we then run a landslide visibility test across land cover types and constrain the relevant inventorying uncertainty. We then present the temporal variability of landslide occurrence in different historical phases of land cover evolution and explore: (i) correlations with climatic indices; and (ii) land cover effects across lithologies. We conclude by replicating the post-2000 inventorying procedure at lower temporal resolution and discuss how prior inferences and correlations become affected.

4. Results

4.1. Hydro-meteorological forcing (1950–2018)

The combined time series of annual precipitation anomaly at Piancaldoli (500 m a.s.l.; from 1950 to 1964) and San Clemente (166 m a.s.l.; from 1965 to 2018) stations (Fig. A.3a) starts with a high positive value in 1951. Subsequently, we observe that the 3- and 5-yr moving averages describe a negative trend in 1953–57, which shifts to positive until 1984 (with some isolated exceptions), in agreement with climate deterioration and concurrent glacier advance recorded in the Alps (e.g., Patzelt, 1985; Hoelzle et al., 2003; Scotti et al., 2014). The trend reverses to a 10-yr negative cycle, with negative anomalies until 1995, then followed by a series of alternating weak positive and stronger negative, 3-to-5 yr cycles.

Annual precipitation and anomalies based on E-OBS data (Figs. 3a and A.3b) display a very similar historical trend of variation – the only exception being the 1953–1965 period, where a more pronounced positive trend is observed (i.e., highest anomalies in 1959 and 1960) – indicating they are suitable to represent the historical hydro-meteorological forcing of the area. Overall, annual precipitation shows a negative significant trend at the 0.05 confidence level (Sen slope = −2.364 and Mann-Kendall (M-K) p-value = 0.030, Table A.1), with highest peak values recorded in 1959 (1263 mm) and 1960 (1295 mm), and the lowest in 1988 (471 mm) (Fig. 3a). Annual maximum daily precipitation (RX1day) does not show a significant trend (Sen slope = 0.080 and M-K p-value = 0.341, Table A.1), however low (i.e., from 1983 to 1988) and high (i.e., from 1989 to 1996) values tend to cluster over time. RX1day ranges from 23 mm in 1985 to 79 mm in 2005, with a mean of 44 mm (Fig. 3b). Precipitation fraction due to extreme events (R99pTOT) appears to increase through time, even though the trend does not score significant at the 0.1 level (Sen slope = 0.080 and M-K p-value = 0.153, Table A.1). R99pTOT displays an average of 16 %, and a maximum of 34 % in 1973. In 1955, 1970, 1974, 1985, 1988 and 1998, null fractional values indicate years without exceptional/extreme rainfall events (Fig. 3c). Clusters of consecutive years (from 3 to 7) with low and high R99pTOT (i.e., between 1996 and 2018) values highlight a short-range correlation (Witt and Malamud, 2013) where periods with and without extreme rainfall events alternate with one another.

4.2. Historical land-cover changes (1853–2018)

Basin-wide, historical land cover mapping (Figs. 4 and A.5) is instructive. In 1853, the basin is mainly covered by transitional shrubs, and subordinately by managed forest and orchards, with limited arable crops (Figs. 5a and A.5). As mentioned earlier, the 1853 historical mapping does not distinguish badlands from the neighbouring land-cover types; this limits our ability to assess badlands area change before 1954, between 1853 and 1954, we observe a sharp increase in arable crops (and pasture), and to a lesser extent of managed forest, at the expense of transitional shrubland (Fig. 5a). Subsequently, between 1954 and 1976 cropland continues to grow (even though at a much slower rate) with a symmetrical decrease of transitional shrubs, whereas forests and badlands remain substantially stable (Fig. 4). The latter extent continues to be stable until today. The 1976–1994 period displays dynamics of agricultural land abandonment. Accordingly, arable crops for the first time start shrinking and transitional shrubs continue to do so, this time compensated by a revived increase in coppice-managed forest (Fig. 5a). From 1994, changes across categories are minimal and the land cover spatial configuration remains about stable.

Land cover spatial distribution over time varies across lithologies (Fig. 5b-e) and therefore some differences may be observed in comparison with basin-wide historical trends. For example, between 1954 and 1976, major changes involved an increase in arable crops in all lithologies – evidence of increasing agricultural pressure – and decrease of transitional shrubs, except in L claystones, where shrubs continue to expand at the expense of managed forest (Fig. 5b). The 1976–1994 period shows common land abandonment dynamics, with decrease of shrubs and arable crops, paralleled by an increase of managed forest and

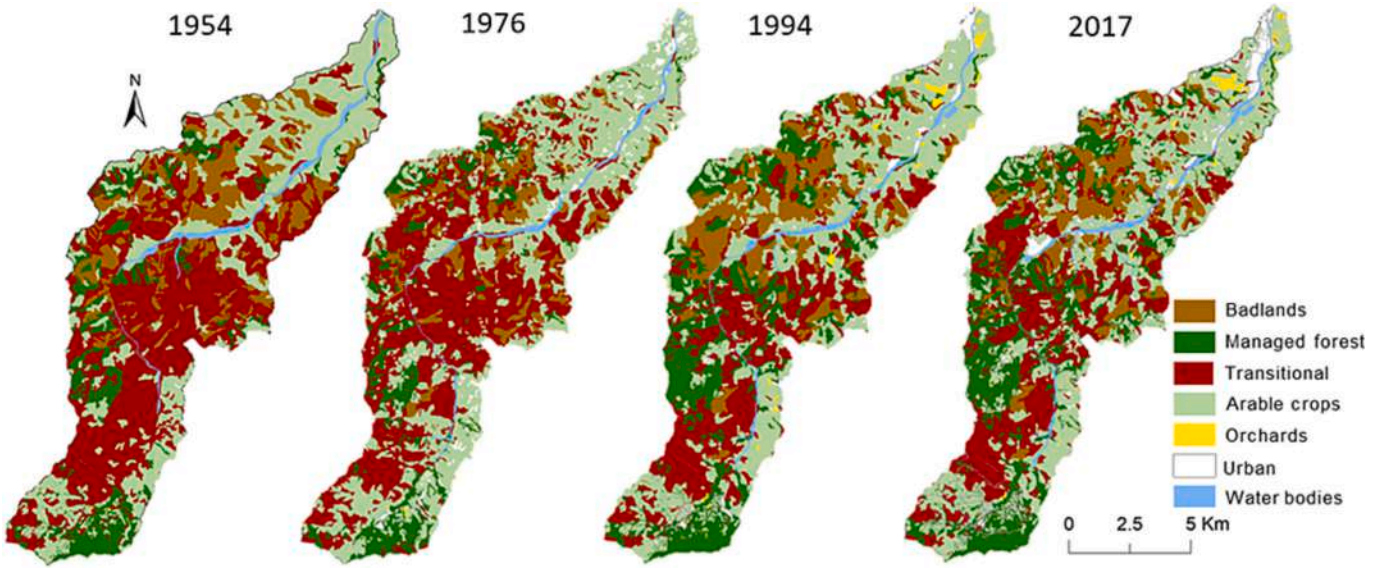

Fig. 4. Land cover maps of the Sillaro River basin in: (a) 1954; (b) 1976; (c) 1994; and (d) 2017.

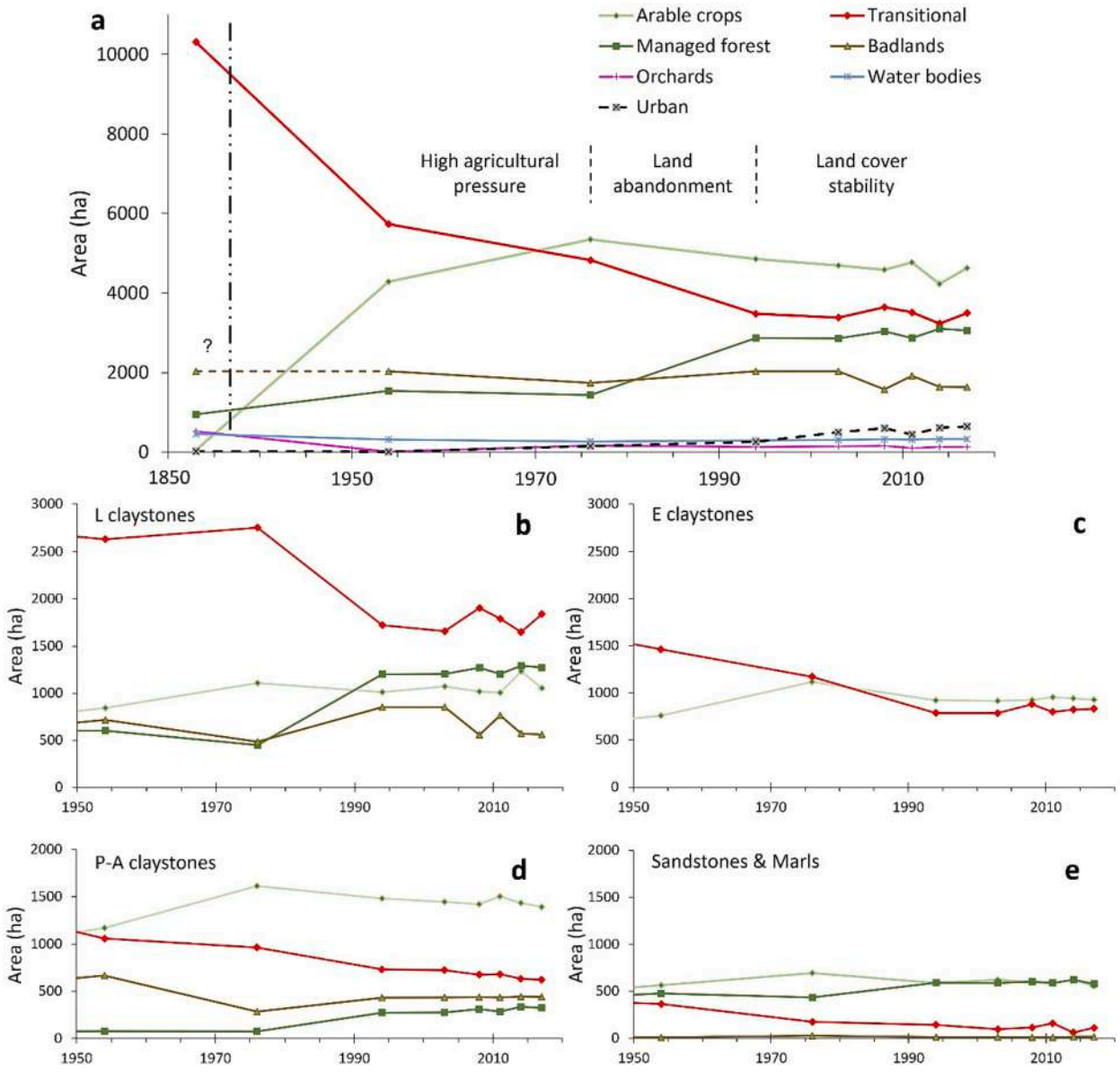

Fig. 5. Historical land-cover changes of the Sillaro River basin (a) and across geologic domains including: (b) Ligurian claystones; (c) Epiligurian claystones; (d) Padano-Adriatic claystones; and (e) Sandstones and marls. In panel a values in 1853 refer to 88 % of the basin area, excluding the headmost portion. Vertical dashed line marks temporal truncation applied between 1850 and 1950.

badlands, except in sandstones and marls, which bear no significant badland terrain. After 1994, the general basin-wide trend of land-cover stability is confirmed. Exceptions relate to badlands in L claystones, the extent of which drops significantly by 2017.

In view of the foregoing historical changes at the basin scale and across geologic domains, we will examine landslide activity as a function of land cover across four main periods. Before 1954, where temporal information on landslide occurrence is associated with highest uncertainty, between 1954 and 1976, where cropland development (hence agricultural pressure) peaks, between 1976 and 1994, a period characterized by dynamics of land abandonment, and after 1994, a phase of general land-cover stability.

In altitudinal terms, these historical land cover changes show that the post-1976 increase in managed forest occurs at elevations distributed below 600 m (Fig. A.6a), at the expense of transitional shrubs, which in the same period display a symmetrical decrease (Fig. A.6c). Concurrently, after 1976, the decrease in arable crops is focused on elevations comprised between 300 m and 750 m (Fig. A.6e). The altitudinal distribution of badlands does not show any significant change through time and peaks consistently between 200 m and 400 m (Fig. A.6g).

The spatial distribution of land cover types does vary as a function of slope gradient i.e., modal values and skewness towards high slopes. Accordingly, arable crops exhibit lowest modal slope (0.21 m/m) and a tail that extends up to about 0.70 m/m (Fig. A.6f). These two statistics increase progressively across transitional shrubs (mode = 0.28 m/m and tail reaches 0.85 m/m; Fig. A.6d), and managed forest (mode = 0.28 m/m and tail reaches 0.95 m/m; Fig. A.6b). By contrast, the slope distribution in badlands is about symmetrical and exhibits highest modal value (about 0.4 m/m) and a positive tail that touches 0.90 m/m (Fig. A.6h).

The shape of the slope distribution within each land-cover category does not change significantly over time. The only exception applies to arable crops (and meadows), where a secondary peak is temporarily observed at about 0.38 m/m in 1954 (Fig. A.6f), possibly a sign of agricultural activity and livestock encroaching relatively steeper terrain

right after World War Two. With reference to landslide susceptibility, we note that part of the post-1976 coppice-forest expansion observed at the expense of shrubland area involves steep terrain i.e., up to roughly 0.9 m/m (cf., Fig. A.6b and d). In principle, despite limited knowledge on the stabilizing effectiveness of coppice-managed forest (Vergani et al., 2017), this historical shift suggests that after 1976 a portion of relatively steep terrain within the basin could be considered less prone to landsliding due to increased root reinforcement and water interception. To evaluate the extent to which historical afforestation may promote slope stability on earth slide/flow dominated terrain, we will examine historical changes in landslide density across land-cover types.

4.3. Landslide activity across lithologies

We mapped 1164 landslides, 345 episodic and 819 recurring, for a combined area (i.e., initiation and transportation) of about 4.4 km^2 (Fig. 1a). At single landslide sites, the number of recurrences ranges from 1 to 9 (Figs. 1b, 6b and c). Landslides are dominantly of the earthflow type (n = 1022), followed by earth slides (n = 129) and complex ones (n = 13). Most of the movements (96 %) occur in clay-dominated lithologies (i.e., 35 % in L claystones, 35 % in E claystones, and 26 % in P-A claystones), and a remaining 4 % is associated with sandstones and marls.

In all lithologies, recurring movements (i.e., recurring landslides) at a location during the study period dominate over single occurrences (i.e., episodic landslides). This dominance is particularly evident in sandstones and marls – where the recurring type represents the 86 % – and tends to weaken across L and E claystones (74 %) and P-A claystones (60 %) (Fig. 6a and Table A.2). Landslide count standardized by the relevant terrain extent (i.e., landslide density) provides a more reliable view of possible lithologic effects on landslide activity (Fig. 6a). Accordingly, clay-dominated lithologies record highest landslide densities, with E claystones displaying a maximum high of 12.3 landslides per km^2, followed by L (7.9 #/km^2) and P-A (7.7 #/km^2) claystones, and lastly by sandstones and marls (2.9 #/km^2) (Table A.2).

The number of recurrences (i.e., activations) at a site records a maximum of 9 in L claystones, 8 in E claystones, 7 in sandstones and marls, and 6 in P-A claystones (Fig. 6b and c). Cumulative frequency distributions show striking overlap among claystones, which follow a non-linear increase, with >160 landslide sites per claystone type (between 80 % and 90 %, depending on the type) that have recorded <4 activations (Fig. 6b). In sandstones and marls, whose cumulative frequency increases linearly, this figure drops by an order of magnitude, to about 10 landslides (<65 %), in agreement with counts and densities shown in Fig. 6a. When considering cumulative landslide areas across number of activations, the different absolute contribution of each

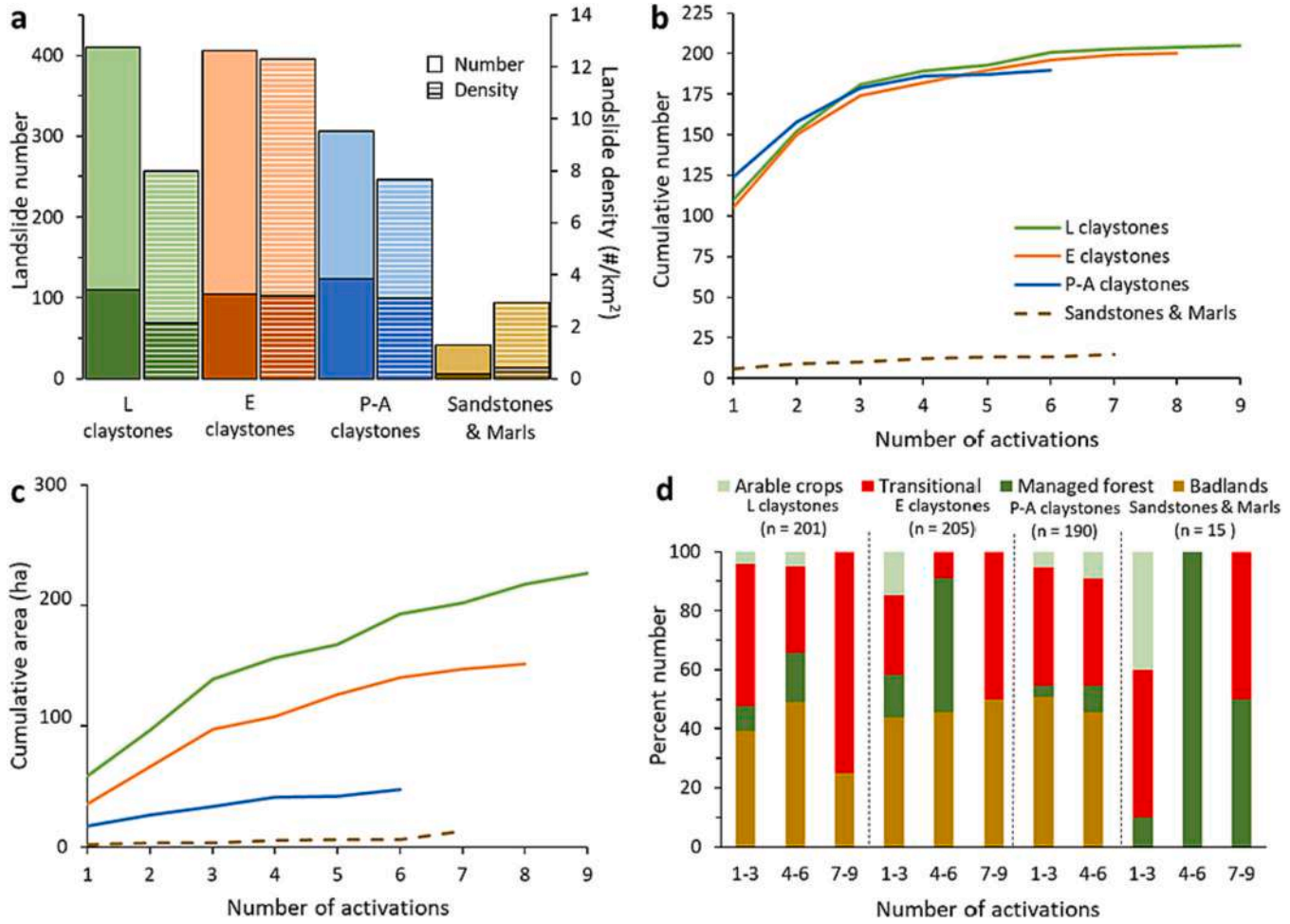

Fig. 6. (a) Number of landslides (filled bars) and landslide density (hatched bars) across geologic domains. Dark tones indicate episodic landslides; lighter tones indicate recurring landslides. Cumulative frequency distributions as a function of landslide activations (i.e., recurrences) at initiation sites across geologic domains, represented by: (b) number of observations; and (c) combined landslide area. (d) Distribution of multiple landslide activations across land cover types in each geologic domain. Numbers refer to sites that have experienced multiple landslide activations in the study period. At sites with recurring activity, we consider landslide activations only those morphological changes, detected on aerial photos, which are associated with the appearance of new distinct headscarps and/or deposition lobes (see text in Section 3 for more details).

claystone type becomes apparent, and the overlap previously observed in landslide count, disappears (Fig. 6c). Specifically, landslides in L claystones make up the largest combined area (227 ha), followed by E claystones (152 ha), P-A claystones (47 ha), and finally by landslides occurred in sandstones and marls (13 ha). Stratification of recurring activations by land cover type across dominant lithologies shows that the largest proportions of 4-to-9 recurrences in claystones are associated with badlands and transitional shrubs (see percentages in classes 4–6 and 7–9 in Fig. 6d); in sandstones and marls (i.e., note that the number of sites is limited to 15 cases), where no badlands are found, high rates of recurring activity dominantly clusters on managed forest and transitional shrubs.

4.4. Land cover and landslide visibility through time

Landslides occur especially on badlands (43 %), transitional shrubland (36 %), and to a lesser extent in managed forest (14 %) and arable crops (7 %) (Table 3). Such percentages, reported for completeness, should not guide any inference on possible land-cover effects, as these may be biased by: (i) the varying degree of landslide (footprint) visibility in different land-cover types (e.g., Pyles and Froehlich, 1987), and the time scales associated with vegetation regrowth on a scar; (ii) the areal extent of different land-cover types within the basin (Fig. 5); and (iii) possible interactions between land cover and lithology (e.g., Jakob, 2000; Brardinoni et al., 2003a). The question of landslide visibility through time will be addressed in this section, the others are the focus of Section 4.5.

To investigate the time window associated with landslide visibility across sequential photo sets, we selected 68 landslides that first appeared (and/or last recurred) in photo years 2006 ($n = 52$), 2008 (n = 10), 2011 ($n = 2$) and 2014 ($n = 4$), and evaluated through time (i.e., 2008, 2011, 2014, 2016, 2018, 2020, and 2022) our ability to identify and map: (i) the entire landslide polygon outline (i.e., initiation and transport zones are “fully visible”); (ii) a portion of it (“partly visible”); or (iii) not at all (“not visible”), chiefly due to vegetation regrowth, in conjunction with other obliteration mechanisms (Fig. 7). Considering the time interval that separates each of the eight photo sets from the next, temporal uncertainty varies from a minimum of 2 years to a maximum of 6 years (i.e., antecedent photo set for landslides first detected in 2006 is photo year 2000), and an average of 3 years. Sample landslides range in size between 330 m^2 to 20,600 m^2. Of these, 24 occur in shrublands, 22 in managed forests, and 22 within badlands.

When representing the percent number of fully and partly visible footprints as a function of time since first appearance, we find that after 2 years, 59 % of the landslides is still entirely visible, and that an additional 21 % remains visible only in part (Fig. 8a). Complete visibility drops to 28 % (+27 % partly visible) after 5 years and to 13 % (+14 % partly visible) after 8 years. After 10 years, complete visibility - hence our ability to delineate the polygon outline - becomes rare (6 %), with an additional 11 % of landslides that are still partly visible (Fig. 8a). Considering the 3-year average uncertainty noted above, complete visibility becomes rare after about 13 years (i.e., 16 when applying the most conservative approach). Landslide persistence through time did not appear to increase directly with landslide size, as median area of fully and partly visible scars does not increase with years since first detection on aerial photo (Fig. A.7).

Landslide stratification by land-cover conditions at initiation (i.e., transitional shrubs, managed forest, and badlands) yields some differences in the time windows associated with complete and partial visibility. The former, whose trend declines non-linearly through time in all three instances, may be achieved in roughly 1 out of 10 cases after 8 years in transitional shrubs (8 %) and after 10 years in badlands (9 %) and forested terrain (9 %) (i.e., descent is steeper in shrubs and gentler in managed forest) (Fig. 8b). Owing to the 3-year average temporal uncertainty, we consider that complete visibility becomes rare (hence mapping unreliable) respectively after about 13 years in transitional shrubs, and after 17 years in badlands and in managed forest. These visibility time windows will be applied to landslides of the inventory identified and mapped in photo year 1954.

Partial visibility functions, which in Fig. 8 are graphically added to the full visibility ones, exhibit temporal trends that differ between land-cover types. In light of the above-mentioned temporal separation between sequential photosets in the 2000–2022 period, the following time scales should be considered with an average temporal uncertainty of 3 additional years. In managed forest, the declining trend mimics closely that of the complete visibility counterpart, with a consistent offset of about 15 %. In practical terms, this implies that after 8 (+3) years 1 landslide out of 7 will remain fully visible and another 1 partly visible (i.e., 14 % fully visible +14 % partly visible) (Fig. 8b). In other words, the latter can be detected but not mapped properly. In badlands, and even more so in shrubs, partial visibility rates remain comparably higher than forested counterparts for the first 5 (+3) years i.e., respectively 59 % (36 % fully visible +23 % partly visible) and 75 % (25 % fully visible +50 % partly visible) (Fig. 8b), and then decline rapidly. After 8 (+3) years, on one hand full and partial visibility functions in badlands overlap, implying that the number of the latter type becomes about negligible; on the other hand, the relevant counterpart in shrubs converges, then completely overlap, with that of managed forest, indicating a comparable hiding effect associated by the two land cover types. After 14 (+3) years, about 15 % of the mapped landslides in shrubland and managed forest are still partly visible, this figure drops to about 5 % in badlands.

4.5. Temporal variability

In photo year 1954, for which we have constrained, depending on land cover type, a maximum visibility window comprised between 13 and 17 years (Fig. 8b), we detected a total of 88 landslides (Table A.3). This figure nearly doubles ($n = 148$) in photo year 1969 (Fig. 9a), during a period of high agricultural pressure that witnessed highest historical cropland extent (Fig. 5) and relatively wetter conditions (see cumulative PRCPTOT in Figs. 3a and 9a). From 1970 through 1996, in a period of land abandonment, with highest recorded expansion of forest cover and concurrent contraction of shrubland (Fig. 5a), we observe a steady decline in landslide occurrences. Subsequently, between 1997 and 2018, a period of generalized land cover stability (Fig. 5a), drier conditions (cumulative PRCPTOT), and precipitation increasingly focused on high-magnitude low-frequency events (mean R99pTOT in Figs. 3c and 9a), we observe a high variability in landslide activity, with an historical high of 203 landslides between 2008 and 2011.

The temporal variability of total landslide area displays similarities with the variation of landslide count, but also differs in many respects (Fig. 9b). First, highest total area is recorded in 1969 (82 ha), as opposed to 2011 for landslide count (Table A.3). Second, the progressive decline in landslide count observed between 1969 and 1996, is now interrupted

Table 3
Number of landslides mapped across land-cover types. Landslides on 1954 aerial photos are noted to allow separation from those identified on higher resolution aerial photos.

		Total	Badlands	Managed forest	Transitional	Arable crops
No. of landslides	<1954	88	45 (51 %)	15 (17 %)	26 (30 %)	2 (2 %)
	1969–2018	1076	454 (42 %)	153 (14 %)	394 (37 %)	75 (7 %)
	All	1164	499 (43 %)	168 (14 %)	420 (36 %)	77 (7 %)

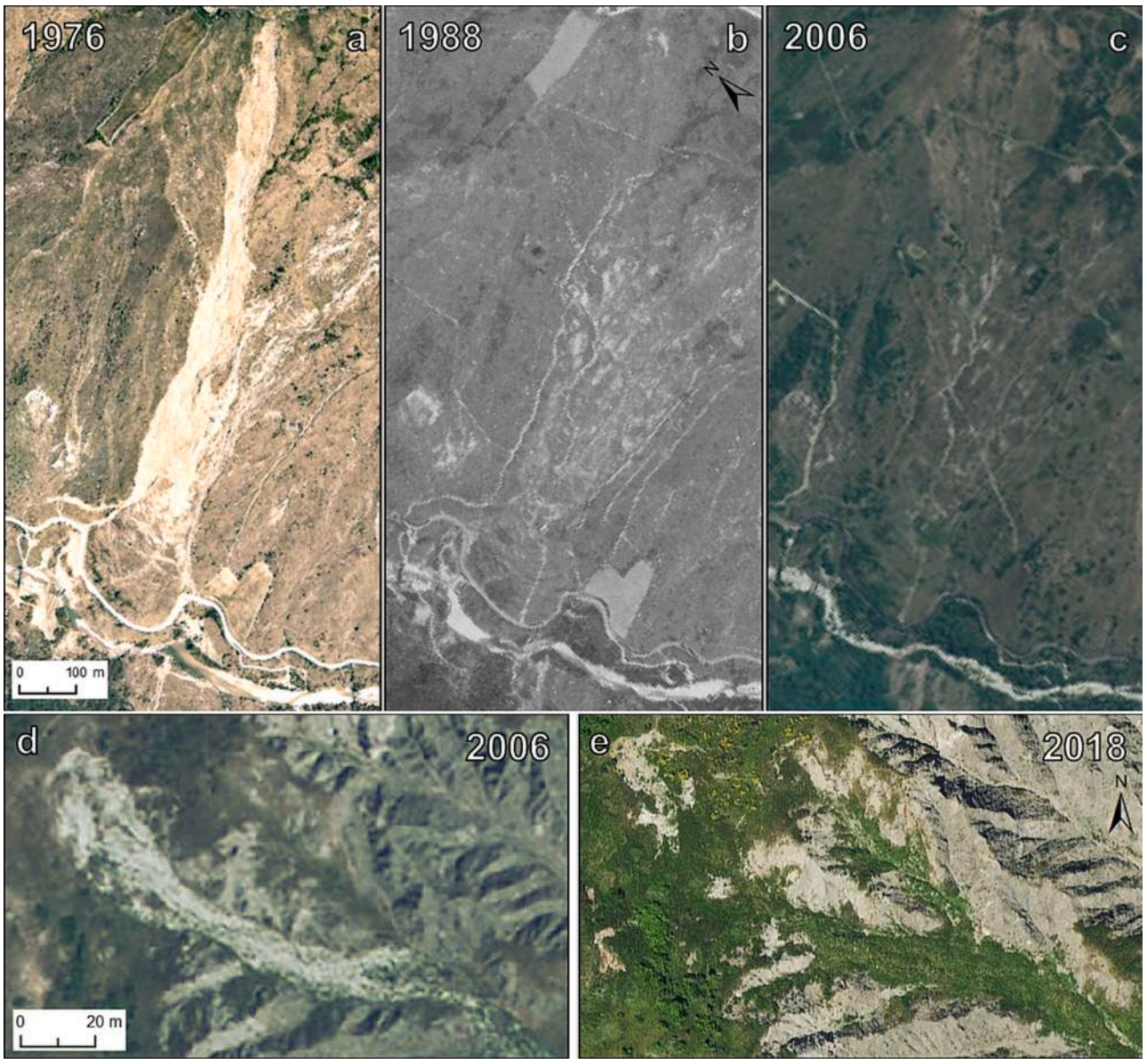

Fig. 7. Example of a large earth flow developed in shrubland: (a) first detected in photo year 1976, and subsequently difficult to delineate in (b) 1988; and (c) 2006, due to progressive revegetation of the erosional scar. Example of a small channelized earth flow occurred in a sparsely vegetated badland system: (d) first detected in photo year 2006; and (e) fully masked by vegetation regrowth in 2018.

in photo year 1988, mainly resulting from a drop in recurring landslide area recorded in photo year 1976. Third, the 1997–2018 period is still characterized by ample temporal variability, but the relative weight of these time intervals in the combined historical (1954–2018) area budget is far less important than how observed in terms of landslide count i.e., 35 ha in 2011 versus 82 ha in 1969. These drops in combined area (i.e., 1988 and 2008) are associated with periods characterized by relatively smaller landslides, as indicated by the historical trend of median landslide area (black dots in Fig. 9b). In this context, an overall trend towards smaller landslides in more recent years is observed. When considering episodic and recurring landslides separately, we observe that the number and area of the latter type are consistently higher than episodic counterparts across all time intervals (Fig. 9) – except in photo year 2016 (see ratios in Table A.3) – and display broader fluctuations across the historical time series.

To detect possible environmental controls, we have examined landslide occurrence in conjunction with land-cover changes and across geologic domains (Fig. 10). In light of the historical land cover dynamics detailed earlier (i.e., Fig. 5), landslide density though time has been analysed across four time periods, each covering about two decades: before 1954, 1955–1976, 1977–1996, and 1997–2018. In each period, landslide density has been standardized by the areal extent of each land cover category and by the relevant number of years.

Results stratified by land cover across the four time steps confirm that landslide densities in clayey lithologies are markedly higher than in sandstones and marls (cf., Figs. 10 and 6a), and that this behaviour may be chiefly associated with the lack of badlands therein (Fig. 10). Indeed, in clayey lithologies densities are consistently highest through time within badlands, followed by transitional shrubland, manged forest and arable crops (Table 4 and Fig. 10a through c). In particular, different claystones share a common historical trend in overall activity (i.e., combined height of each stacked bar). Accordingly, after 1954 landslide density increases in the 1955–1976 period, characterized by maximum anthropogenic pressure and relatively wetter conditions, it decreases in the 1977–1996 period, characterized by land abandonment dynamics, and peaks sharply between 1997 and 2018, during a period of

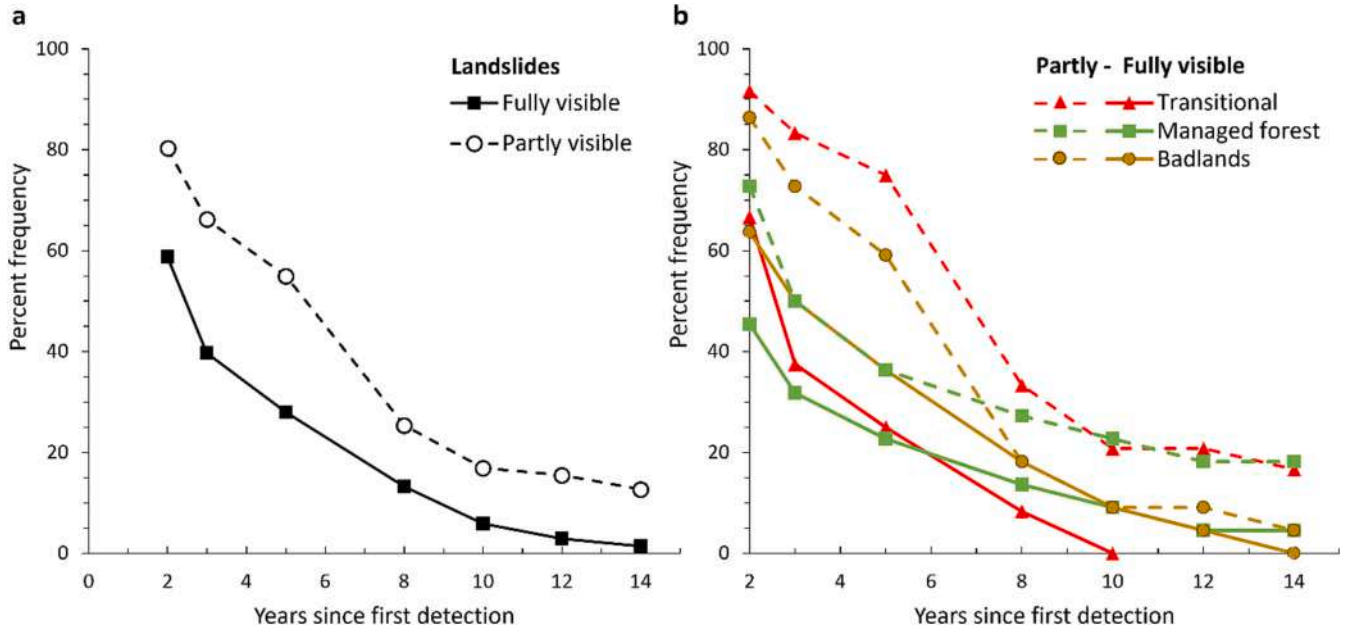

Fig. 8. Proportion of landslides (expressed as percent frequency) that respectively remain fully visible (solid linework) and partly visible (dashed linework) as a function of time since first detection in aerial photos: (a) considering all 68 landslides together; and (b) stratifying landslides by land cover conditions at initiation (i.e., transitional shrubs, managed forest, and badlands). Note that partial visibility functions are represented in additive fashion with respect to the fully visible counterparts. For example, after 2 years we observe that 60 % of the landslides detected are entirely visible, and that an additional 20 % remain partly visible, for a combined percentage of 80 % (panel a). In the text, visibility functions are described in relation to the uncertainty associated with the temporal spacing of the photo sets utilized (i.e., 2006, 2008, 2011, 2014, 2016, 2018, 2020, 2022) and considering the antecedent photo set (i.e., 2000). Average uncertainty would add 3 extra years (i.e., the average spacing between the study photo sets between 2000 and 2022); maximum (most conservative) uncertainty would add 6 extra years (i.e., the time difference between 2000 and 2006).

generalized land cover stability as well as drier conditions, with precipitation increasingly falling during high-magnitude low-frequency events (Table 4). This historical trend is also shared by landslide densities considered in badlands, managed forest and croplands separately, whereas transitional shrubs, regardless of lithology, display a progressive increase through time (Table 4). By contrast, landslide densities in sandstones and marls: (i) score highest in managed forest, followed by transitional shrubland and arable crops (Fig. 10d); and (ii) increase progressively through time (Table 4 and Fig. 10d).

5. Discussion

5.1. Lithologic effects

With reference to the first objective, we document a strong lithologic control on historical landslide occurrence and recurrence. When considering landslide density per unit lithologic area as a proxy, landslide activity is 3 to 4 times higher in the Ligurian Allochthonous Complex (i.e., L and E claystones) than in the Flysch Complex (i.e., sandstones and marls) (Table A.2, and Fig. 6a). This 4 to 1 ratio agrees with prior findings of an inventory conducted on 1954 aerial photos across the same geologic complexes in the Central and Northern Apennines (Guzzetti et al., 1996). In this context, our multi-temporal classification into episodic and recurring slope failures allows adding that (i) landslide activity at a site in a roughly 80-year time window can recur up to 9 times (Fig. 6b and c); and that (ii) the relative importance of recurring landslide sites, both numerically and areally, varies with lithology. In particular, recurring landslide sites can account respectively for 35 % (P-A claystones) to 60 % (sandstones and marls) of the total landslide count, and for 65 % (P-A claystones) to 90 % (sandstones and marls) of the total landslide area, with L and E claystones displaying intermediate percentages (Fig. 6a). We further show that this lithologic variability, partly depends on land cover conditions. In claystones, sites characterized by most frequent activations (i.e., four times and higher) occur on badlands and transitional shrubs (Fig. 6d); in sandstones and marls, where locally no badlands are found, activations are sensibly more frequent in coppice managed forest (Fig. 6d), namely at those sites where clay-rich marls outcrop. The high rates of recurrence in transitional shrubs across claystones suggests that, despite post-disturbance vegetation establishment, rooting depths at such sites may be shallow, with minimal establishment of deeper-rooted tree species in charge of slope reinforcement (Buma and Pawlik, 2021).

5.2. Time scales of landslide visibility and inventorying uncertainty

With respect to the second paper objective, concerned with the assessment of the mapping uncertainty as a function of temporal resolution, our multi-temporal visibility test allowed constraining the time windows for which, the landslide initiation and transport zones could be consistently identified and/or mapped across sequential photosets (Fig. 8). While identification of new landslides may be achieved even when scars are only partly visible due to vegetation regrowth, the mapping of the entire landslide footprint requires that the initiation and transportation zones be completely visible. Complete visibility is critical for evaluating landslide sediment fluxes (e.g., Reid and Dunne, 1996; Dadson et al., 2004; Brardinoni et al., 2009, 2012), as well as for constraining landslide magnitude-frequency relations (e.g., Stark and Hovius, 2001; Brardinoni and Church, 2004; Bell et al., 2012). Partial visibility remains extremely valuable for addressing applied issues that rely on the best possible historical record of landslide occurrence, regardless of landslide size, such as the assessment of landslide susceptibility (e.g., Hussin et al., 2016; Pisano et al., 2017) and the definition of precipitation thresholds (e.g., Caine, 1980; Guzzetti et al., 2008; Berti et al., 2012; Zêzere et al., 2015).

We find that complete visibility sets at 59 % and that an additional 21 % of the scars are still partly visible after about 2 years from first detection on aerial photos, which become 5 when considering the 3 extra years associated with the average temporal uncertainty of the

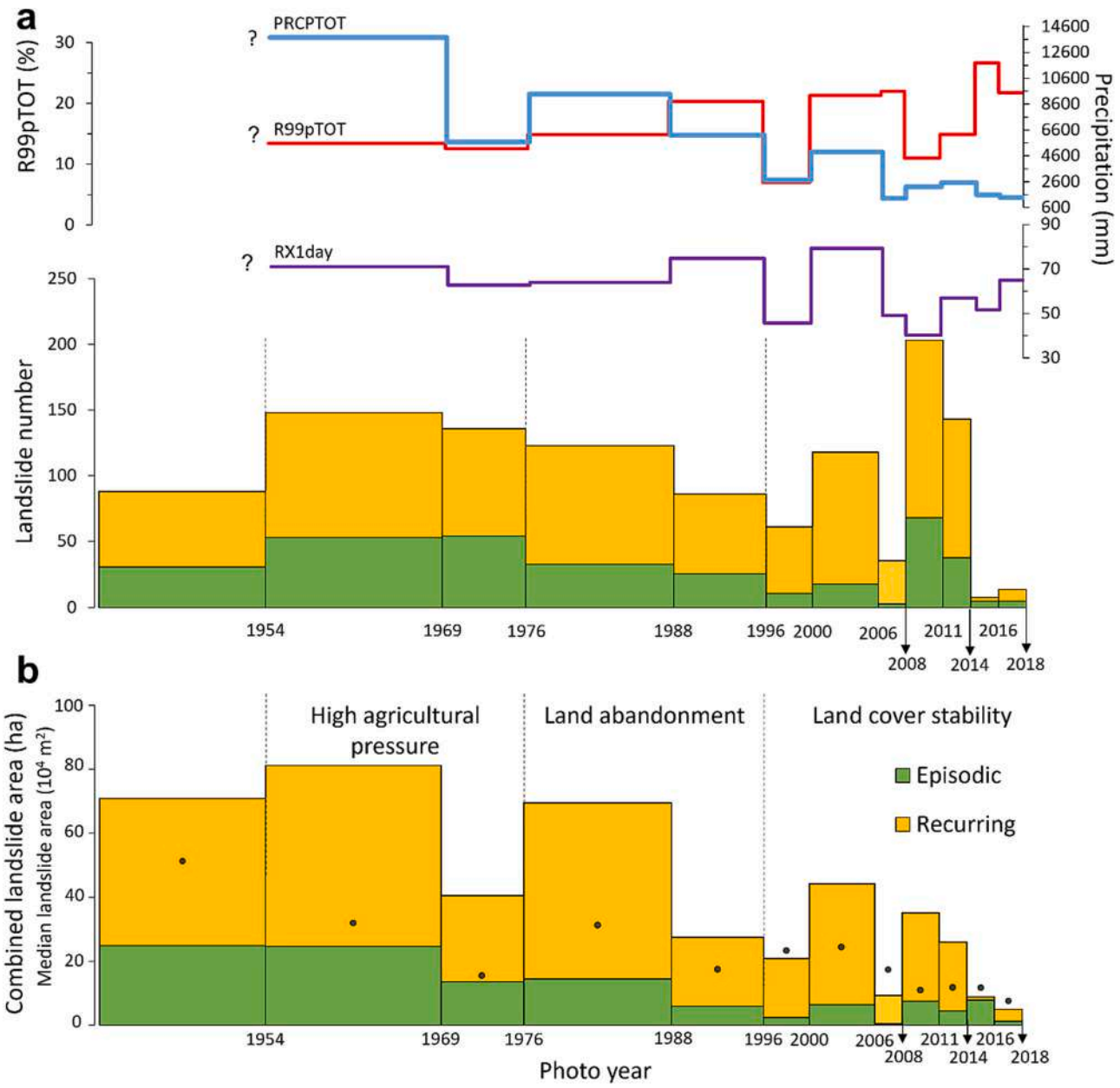

Fig. 9. Variability in the (a) number of landslides, and (b) relevant area across time periods bound by historical photo sets used in this study. Green bars indicate episodic landslides; yellow bars indicate recurring landslides. In panel a, linework indicates concurrent variation in cumulative total precipitation (cumulative PRCPTOT; blue), maximum daily precipitation (maximum RX1DAY; violet), and the mean precipitation fraction (%) due to extremely wet days (mean R99pTOT; red) i.e., when daily precipitation amount exceeds the 99th percentile in the 1950–2020 period. In panel b, black dots indicate median landslide areas. (For interpretation of the references to colour in this figure legend, the reader is referred to the web version of this article.)

actual landslide occurrence. This finding implies that in settings of the Northern Apennines, inventories compiled at a 5-year temporal resolution may be missing up to 20 % of the actual landslide scars, and that the size (i.e., area) of an additional 21 % of them may be underestimated. After 8 (+3 years), full visibility drops to 13 % – without considering an additional 14 % of scars that remain partly visible – and testifies to the degree of (in)completeness that may affect an inventory compiled at decadal temporal resolution. These changes of landslide scar persistence through time vary with land cover conditions at initiation (Fig. 8b). Accordingly, a decadal-resolution inventory – comparable with the visibility conditions constrained in Fig. 8b after 8 (+3) years – would include the entire footprint of about 18 % of the actual scars occurred in badlands, 14 % in managed forest, and only about 8 % in transitional shrubs. In terms of partly visible scars, after about 8 (+3 years): (i) their number becomes negligible in badlands (i.e., the fully and the additive partly visible functions overlap); and (ii) the declining trend in shrubs converges, then completely overlap with that of managed forest (Fig. 8b). In consideration of the 15- to 30-year turn over adopted locally in coppice forest practices the latter observation suggests that after about a decade shrubs become as efficient as managed forest cover at preventing reliable landslide detection and mapping.

Overall, the time window required for the complete or partial obliteration of all scars ranges from a minimum of 13 (10 + 3) years in transitional shrubs, to 17 (14 + 3) years in badlands, and at least 17 years in managed forest (Fig. 8b). The recovery pace in shrubland closely matches the 12 years documented for post-landslide grassland regeneration in the Aso volcano area, Japan (Saito et al., 2022), but appears slower than in post-catastrophic earthquake conditions in

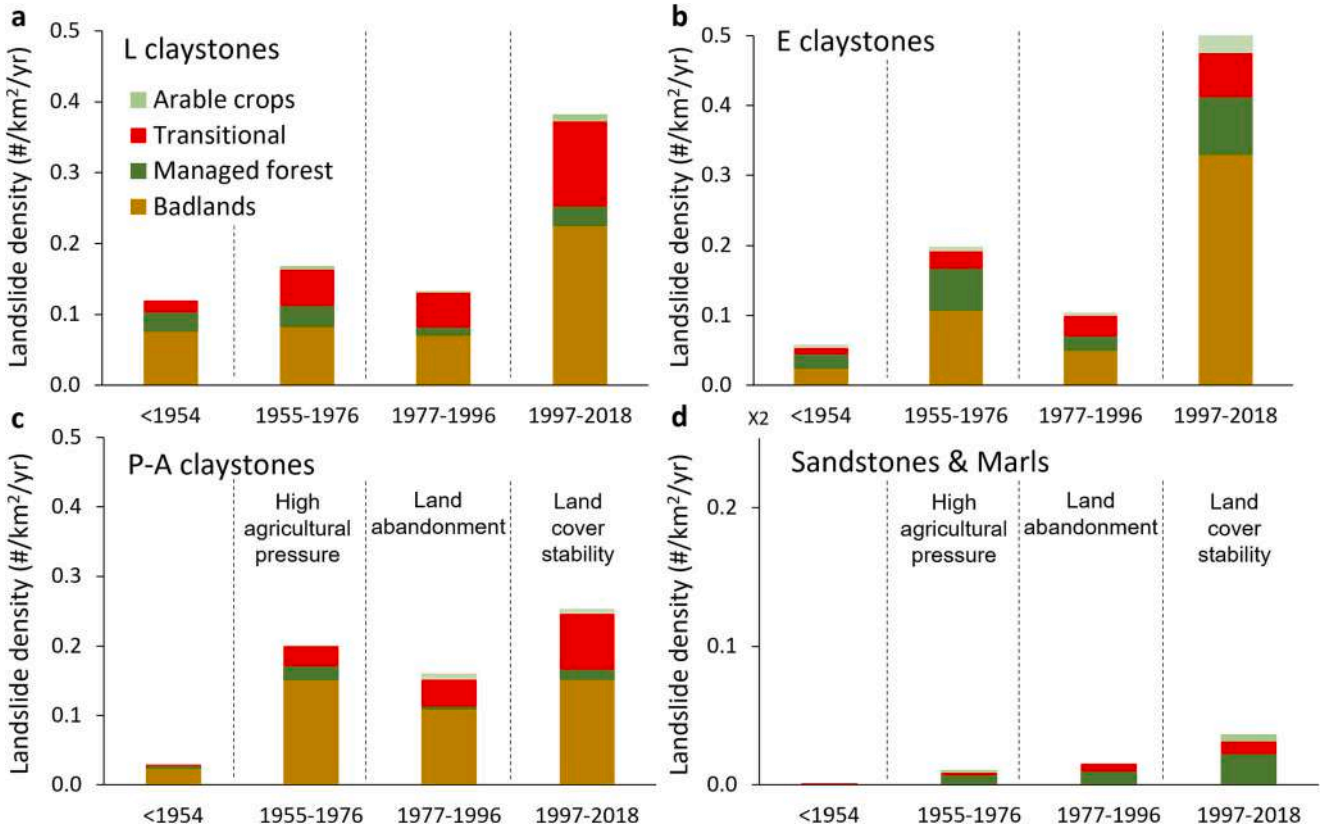

Fig. 10. Stacked bar diagrams showing the historical variation in landslide density, stratified by land cover at landslide initiation, in: (a) L claystones; (b) E claystones; (c) P-A claystones; and (d) Sandstones and marls. Numbers are standardized by basin-wide land cover area and years of observation. Note Y-axis exaggeration in panel d.

Table 4
Historical landslide densities stratified by dominant geology and land cover.

		Landslide density (#/km^2/yr)			
Geology	Land use	<1954	1955–1976	1977–1996	1997–2018
L claystones	Badlands	0.08	0.08	0.07	0.22
	Managed forest	0.03	0.03	0.01	0.03
	Transitional	0.02	0.05	0.05	0.12
	Arable crops	0	0.01	0	0.01
E claystones	Badlands	0.02	0.11	0.05	0.33
	Managed forest	0.02	0.06	0.02	0.08
	Transitional	0.01	0.03	0.03	0.06
	Arable crops	0	0.01	0	0.02
P-A claystones	Badlands	0.02	0.15	0.11	0.15
	Managed forest	0	0.02	0	0.01
	Transitional	0	0.03	0.04	0.08
	Arable crops	0	0	0.01	0.01
Sandstones and marls	Badlands	0	0	0	0
	Managed forest	0	0.01	0.01	0.02
	Transitional	0	0	0.01	0.01
	Arable crops	0	0	0	0.01

central Taiwan, where after 6 years, 86 % of the landslide scars were found to have gradually recovered (Chou et al., 2009). Compared to till-mantled, granitic terrain of coastal British Columbia, where shallow debris slides and debris flows can persist on aerial photos for up to 30–35 years (Rood, 1984; Smith et al., 1986; Brardinoni, 2001), the faster recovery time constrained in the Sillaro River basin would require about twice the number of sequential photosets to obtain an inventory of comparable completeness. Considering that the temporal spacing of aerial photos before 1996 varies between 7 and 15 years, in this period the inventory may be biased by rates of undersampling that range from 45 % (i.e., 5 + 3 years in the partly visible function in Fig. 8a) to as much as 85 % (i.e., 12 + 3 years in Fig. 8a). Consequently, when evaluating land cover and climatic effects, landslide counts and relevant density values in these time periods (i.e., Figs. 9 and 10) should be considered as minimum estimates.

Notwithstanding the uncertainties associated with the compilation of multi-temporal inventories discussed in this paper, and despite recent developments on the (semi)automated detection and mapping of slope failures following typhoons or catastrophic earthquakes, the visual interpretation of optical stereoscopic aerial images still remains the most effective method to build landslide inventories across decades (Guzzetti et al., 2012; Mondini et al., 2011, 2021). Indeed, the availability of

aerial stereoscopic coverages (starting from 1927 in Italy, source: IGM, 2023), along with their expert interpretation, guarantees a medium- to long-term evaluation of landslide occurrence over time, their accurate mapping and feature characterization.

5.3. Correlation with hydro-meteorological forcing

To evaluate to what extent historical landslide activity in the Sillaro River basin might respond to hydro-meteorological forcing (e.g., Berti et al., 2012; Ciccarese et al., 2020; Luna and Korup; 2023), we have calculated three climatic precipitation indices (i.e., cumulative PRCPTOT, maximum RX1DAY and mean R99pTOT) (see Sections 3 and 4.1) across the time intervals that characterize the sequential photo sets (Table 1). Qualitatively, the historical trend in cumulative total precipitation (PRCPTOT), which displays an overall decline (in agreement with Fig. 3a), appears to mimic closely that of landslide area (Fig. 9b), and to a lesser extent, that of landslide frequency (Fig. 9a). Simultaneously, despite higher noise, we observe that the relative weight of mean extreme precipitation events (R99pTOT) displays an opposite trend (i.e., increases), suggesting that as total precipitation decreases, extreme events become progressively more important (in agreement with Fig. 3c). Annual maximum daily precipitation (RX1day) does not exhibit a clear tendency (Figs. 3b and 9a).

The foregoing qualitative observations are corroborated by simple correlation analysis, which, due to incomplete gridded precipitation data, excludes the pre-1954 period. Accordingly, landslide count (corr. coeff. = 0.441; not significant at 0.1 level) and especially landslide area (0.927; significant at 0.001 level) are directly related to PRCPTOT, and consequently, inversely related to R99pTOT (Table 5). In this latter case, correlation is stronger for landslide count (−0.625; significant at 0.05 level) than for landslide area (−0.425; not significant at 0.1 level). While the latter finding may legitimate the use of historical landslide catalogues/archives for evaluating climatic controls on landslide occurrence (Rossi et al., 2010; Witt et al., 2010), the strength of the correlation between landslide area and total annual precipitation highlights the value of compiling landslide multi-temporal inventories, and the way in which initiation and transportation zones were outlined and separated from deposition zones. When considering, episodic and recurring landslides separately, correlations change very little (Tables A.4 and A.5).

5.4. Historical land abandonment, climate change, and the geomorphic significance of badlands

Evaluation of basin-wide historical landslide density in relation to historical land cover changes (Fig. 10 and Table 4) and precipitation trends (Figs. 3 and Table A.1) indicates that badlands dominate the scene, and that other historical land cover changes (i.e., the transition from shrubland to managed forest and vice versa) may not be as important at the basin scale. Following this logic, the lack of badlands in sandstones and marls would explain the strong lithologic control on landslide activity noted above, and the 3- to 4-fold increase in landslide density in claystone-dominated contexts. Indeed, badlands are associated with highest historical landslide densities across all four time periods examined, followed by transitional shrubland and by managed forest, which often display comparable values, and lastly by arable crops (Table 4). If one excludes arable crops – considering that seasonal disturbance associated with agricultural practices typically obliterates most of the shallow landslide scars therein – this land cover stability ranking may be interpreted as the combined result of: (i) the stabilizing effect of an increasingly structured and well-developed vegetation cover (Glade, 2003; Sidle and Ochiai, 2006, and references therein); and (ii) the slope frequency distributions of the three land cover types (i.e., modal values and skewness towards high slopes). Accordingly, badlands not only lack of a significant vegetation cover, but also tend to occupy steeper terrain within the landscape (median slope = 0.4 m/m), compared to managed forest and transitional shrubs, whose slope distributions broadly overlap and share lower median values (i.e., 0.28 m/m) (Fig. A.6).

With respect to the inefficacy of forest regeneration at reinforcing slope stability following land abandonment in terraced settings (e.g., Cevasco et al., 2014; Persichillo et al., 2017), we extend results to terrain of the Northern Apennines where agricultural practices did not entail the construction of terraces or other high-maintenance anthropogenic structures. In such settings, we observe that managed forests between 1997 and 2018 – part of which regenerated between 1977 and 1996 – qualify as the most stable land cover category in claystones (Table 4 and Fig. 10). In marls and sandstones, the limited number of observations does not allow to make robust interpretations. To address this question at a more functional and reliable level, further empirical work on the tensile strength afforded by coppice forest is needed (Vergani et al., 2017).

In this context of historical variability, the 1997–2018 period stands out for recording much higher landslide activity, despite the general land cover stability attained after a phase of land abandonment (1977–1996), which involved shrubland transition to forest on steep slopes (cf., Fig. A.6b and d). Compared to the 1955–1976 period – the second most active – between 1997 and 2018 we observe a 2-fold (i.e., P-A claystones) and a 3-fold (i.e., L- and E-claystones) landslide density increase in shrubland and badlands respectively (Table 4). At first sight, this striking increase may be attributed to climate change i.e., the weight of extreme rainfall events has grown highest in an overall drier climate. However, this explanation discounts that between 1997 and 2018 the inventory was compiled at higher temporal resolution. Consequently, the sharp increase in landslide density may just derive from a reduced degree of undersampling.

5.5. Temporal resolution effects

Considering the landslide visibility functions previously constrained (Fig. 8) and the inventory's contrasting temporal resolutions before and after 1996 (Table 1), we expect the latter period to exhibit a higher degree of completeness. In turn, this variability in time resolution may affect relevant inferences made on climatic and land cover effects (Table 4, Figs. 9 and 10). To evaluate the significance of this sampling bias, we replicated the post-1996 multi-temporal mapping at coarser resolution, that is, by considering only the landslides detectable in the 2006 and 2018 photos (Fig. 11). The two “simplified” intervals of respectively 10 (1996–2006) and 12 years (2006–2018) replace the 2- to 6-year resolution of the original time series. To guarantee a coherent temporal comparison between landsliding and climate, the simplified values of landslide count, combined area, and those of the climate indices were then calculated accordingly.

Simplification has the primary effect of hiding part of the landslide and climatic temporal variability. Qualitatively, the original post-1996 increase in landslide number is retained, whereas the declining trend in landslide area is basically lost. In terms of climatic variability, the historical declining trend in PRCPTOT becomes masked (cf. Figs. 3a and 11a), and the tendency of R99pTOT to increase is attenuated (cf. Figs. 3c and 11a). Comparison of pairwise correlation analysis between the original and the simplified temporal sampling shows that landslide area

Table 5
Correlation matrix between the total number of landslides (episodic and recurring) (#LS), relevant combined landslide area (LS area) and precipitation indices. Period of investigation: 1955–2018.

Total LS	#LS	LS area	PRCPTOT	RX1day	R99pTOT
#LS	1.000				
LS area	0.674	1.000			
PRCPTOT	0.441	0.927***	1.000		
RX1day	0.038	0.428	0.568	1.000	
R99pTOT	−0.625*	−0.425	−0.278	0.309	1.000

Level of significance: + <0.1 * <0.05 ** <0.01 *** <0.001.

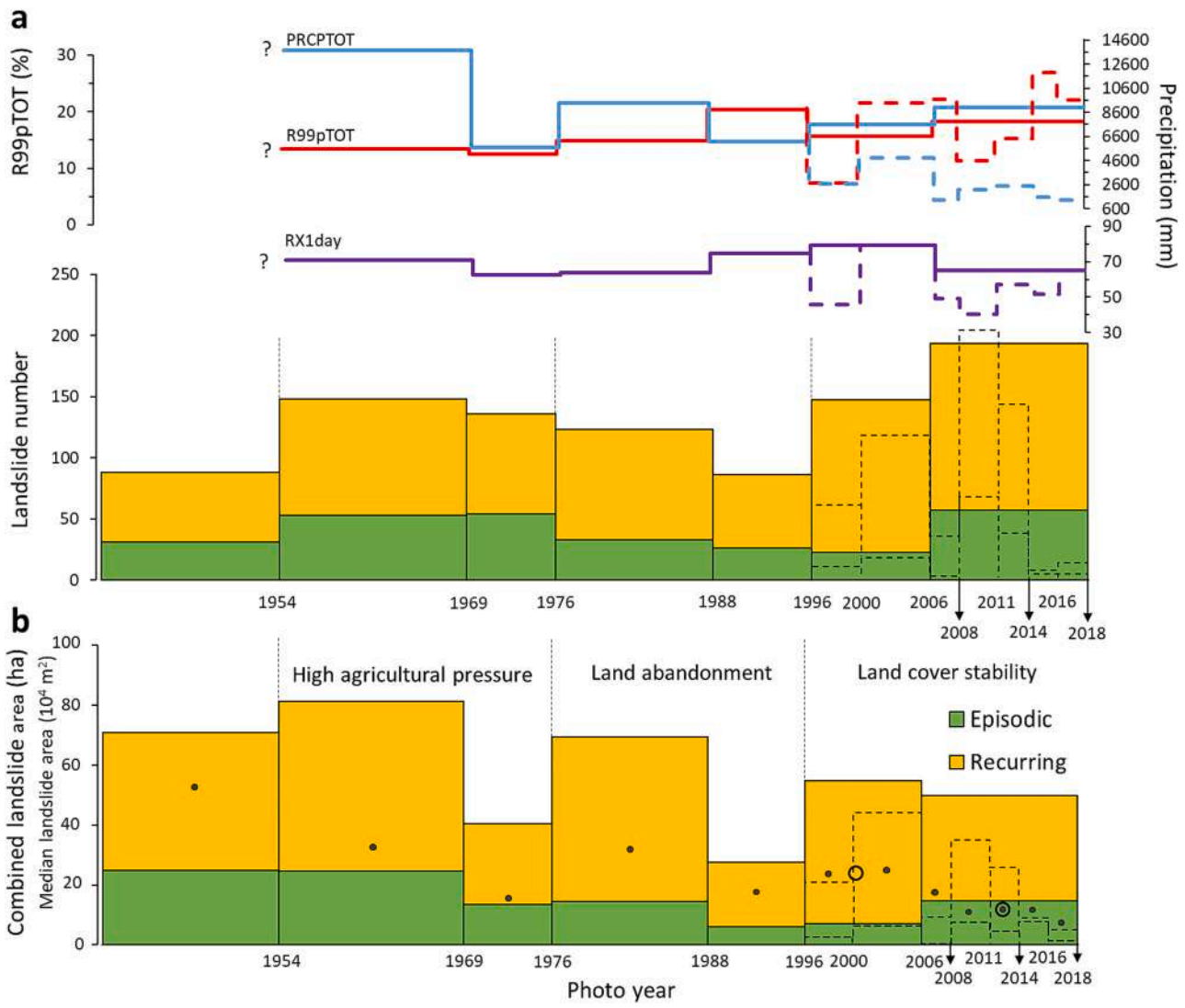

Fig. 11. Temporal variability in the (a) number of landslides, and (b) relevant area across simplified time periods, where post-1996 landslide mapping was limited to photo year 2006 and 2018 only. Green bars indicate episodic landslides; yellow bars indicate recurring landslides. In panel a, coloured linework indicates concurrent variation in cumulative total precipitation (PRCPTOT; blue), maximum daily precipitation (RX1DAY; purple), and the mean precipitation fraction (%) due to extremely wet days (R99pTOT; red) i.e., when daily precipitation amount exceeds the 99th percentile in the 1950–2020 period. Dashed linework indicates landslide and precipitation trends across the original time periods illustrated in Fig. 9. In panel b, black dots and empty circles indicate respectively median landslide areas across the original time periods and across the post-1996 simplified ones. (For interpretation of the references to colour in this figure legend, the reader is referred to the web version of this article.)

remains significantly correlated with PRCPTOT – even though at a lower level of significance (i.e., 0.05) – and that correlation between landslide count and R99pTOT fades (Tables 6 and A.6). On the one hand, this outcome reinforces the value of compiling multi-temporal inventories over the use of historical catalogues/archives, in which, typically, information on landslide size is not recorded. On the other hand, when compared with the correlations shown for the original inventory (Table 6), it underlines the importance of pursuing high temporal resolution products.

With respect to the much higher landslide densities observed in the 1997–2018 period (Fig. 10), the compilation of a simplified inventory – at a resolution consistent with that of the previous time intervals – yields

Table 6
Summary of the correlations between landslide and climatic variables that resulted significant using the original multi-temporal inventory and comparison with the simplified version.

Inventory (photo years)	Landslides	LS area - PRCPTOT		#LS - R99pTOT	
		Corr. type	Significance	Corr. type	Significance
Original (all photo years)	All	Direct	<0.001	Inverse	<0.05
	Episodic	Direct	<0.001	Inverse	<0.05
	Recurring	Direct	<0.001	Inverse	<0.1
Simplified (1969–1976–1988-1996-2006-2018)	All	Direct	<0.05	Inverse	n.s.
	Episodic	Direct	<0.1	Inverse	n.s.
	Recurring	Direct	<0.05	Inverse	n.s.

comparably lower values (Fig. 12). Reduction in landslide density, depending on dominant lithology, ranges from 1.5 to 2.1 times in badlands, from 1.2 to 2 times in transitional shrubs, and from 1.3 to 2 times in managed forests (Table A.7). Overall, we obtain a more balanced picture of post-1996 temporal variability, in which, landslide activity: (i) remains highest in E- and L-claystones, even though to a much lower extent; (ii) increases slightly in sandstones and marls; and (iii) even decreases in P-A claystones, compared to the 1955–76 and 1977–96 periods. When the confounding of variable inventorying resolution is removed, the magnitude of the possible effects induced by climate change is drastically reduced than how originally envisaged.

6. Conclusions

In the Sillaro River basin, we portray a composite history of landslide activity resulting from: (i) lithologic diversity; (ii) historical mismatch between peaks in agricultural pressure and annual precipitation; and (iii) heterogeneous temporal resolution of landslide mapping in relation to landslide persistence through time. Lithology exerts a primary control, in that landslide densities in claystones are 3-to-4 times higher than in marl-sandstone alternations. This difference is chiefly mediated by the spatial distribution of badlands, which represent the most active land cover type. Classification into episodic and recurring landslides shows that the latter type prevails, and that new scars at a site could recur up to nine times within the eight decades examined. Highest rates of recurrence are found primarily in badlands and to a lesser extent in shrubs.

Our work represents a first effort to constrain the time scales involved for consistent landslide detection (i.e., partial visibility) and mapping of the entire scar footprint (i.e., full visibility) across sequential photosets. Accordingly, by constraining landslide visibility functions we provide a first-order evaluation of the uncertainty associated with multi-temporal mapping as a function of temporal resolution, which may be used as correction factor for existing inventories across the Northern Apennines. Taking into account a 3-yr average uncertainty, we show that, after 2 (+3) years from first detection, complete visibility of the scar footprint is achieved in 59 % of the cases, and that an additional 21 % of them remains partly visible. In practical terms, an inventory conducted at a 5-year resolution would miss up to 20 % of the actual landslide scars, and the footprint size of an additional 21 % would result underestimated. After 8 (+3) years, full visibility drops to 13 %, attesting to the degree of undersampling that would affect an inventory compiled at decadal resolution. Proportions of scar persistence through time vary with land cover, with the time window required for complete or partial obliteration of all scars ranging from 13 (10 + 3) years in transitional shrubs, to 17 (14 + 3) years in badlands, and to >17 years in coppice managed forest.

Historical analysis of landslide count and density across land cover types shows: (i) an increase between 1955 and 1976, when both anthropogenic pressure and mean annual precipitation are highest; (ii) a decrease from 1977 through 2000, during land abandonment and concurrent decline in annual precipitation; and (iii) an abrupt peak between 2000 and 2014, within a broader period of generalized land cover stability, characterized by lowest mean annual precipitation and highest inventory resolution. Replication of the post-1996 inventory at coarser time resolution imparts a drop in landslide densities by a factor of 2. Most importantly, we show that when removing the bias introduced by heterogeneous temporal resolution, prior effects attributable to climate change (i.e., the increasing weight of extreme precipitation events) become substantially buffered, underlining the importance of using consistent sampling resolution in multi-temporal studies.

With respect to land cover effects, we find that badlands are

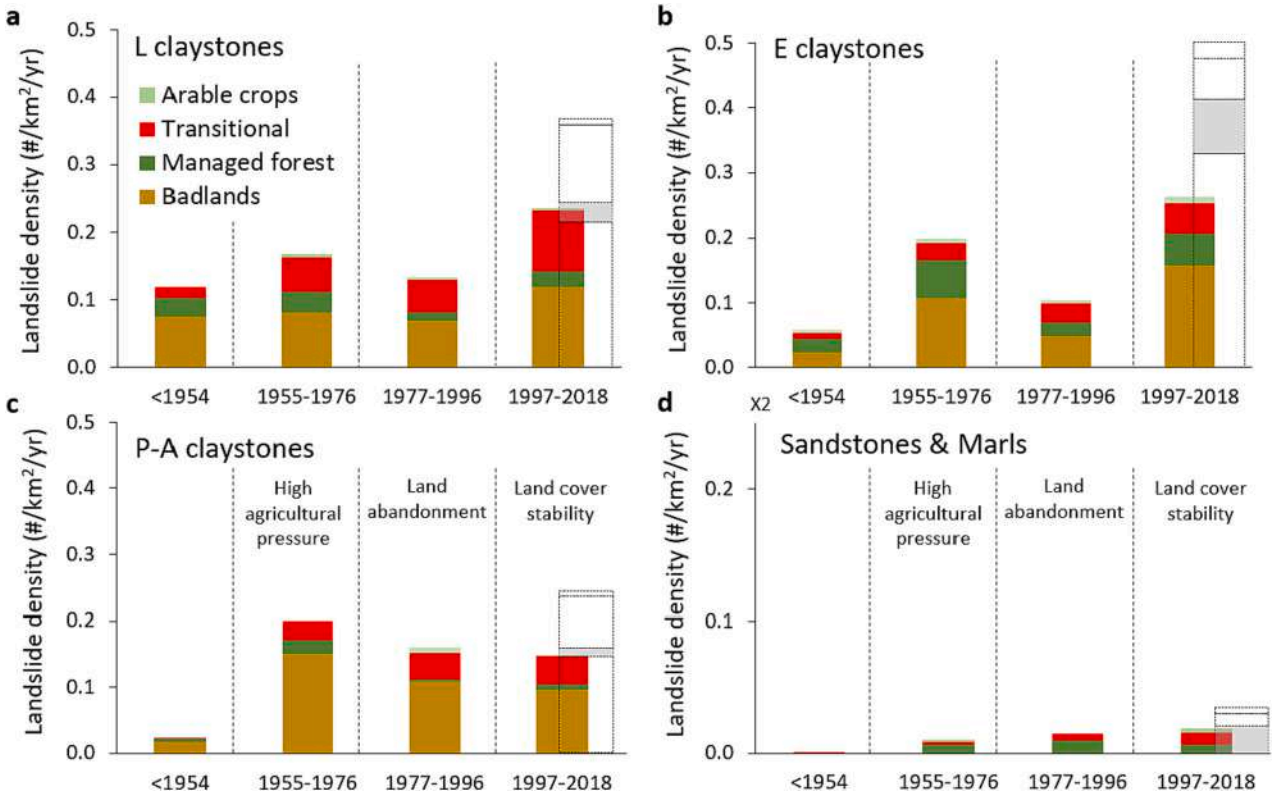

Fig. 12. Stacked bar diagrams showing the historical variation in landslide density associated with the simplified inventory in the 1997–2018 period, stratified by land cover at landslide initiation, in: (a) L claystones; (b) E claystones; (c) P-A claystones; and (d) sandstones and marls. Numbers are standardized by basin-wide land cover area and years of observation. Note Y-axis exaggeration in panel d. Dashed linework indicates landslide density values stratified by land cover at initiation, across the original time periods illustrated in Fig. 10.

associated with highest historical landslide densities, followed by transitional shrubland and by managed forest. We propose that this ranking reflects: (i) the stabilizing effect of an increasingly structured and developed vegetation cover; and (ii) increasing steep topography as one moves from transitional shrubs and managed forest, to badlands, which are distinctively steeper. With reference to prior work pointing to the inefficacy of natural forest regeneration at improving post-abandonment slope stability, we show that in settings with no terracing involved, managed forest between 1997 and 2018 – part of which regenerated between 1977 and 1996 – qualifies as the most stable land cover in claystones, and therefore appears to have an overall stabilizing effect. To assess cascading effects on fluvial adjustment and implications for sustainable sediment management, future work in the Sillaro River basin will integrate field surveys to constrain volumetric rates of sediment transfer and delivery to streams.

CRediT authorship contribution statement

Sharon Pittau: Formal analysis, Investigation, Writing – original draft, Writing – review & editing, Data curation. **Mauro Rossi:** Formal analysis, Writing – original draft, Funding acquisition. **Manel Llena:** Investigation, Validation, Writing – review & editing. **Francesco Brardinoni:** Conceptualization, Formal analysis, Funding acquisition, Investigation, Supervision, Writing – original draft, Writing – review & editing.

Declaration of competing interest

The authors declare that they have no known competing financial interests or personal relationships that could have appeared to influence the work reported in this paper.

Data availability

Data will be made available on request.

Acknowledgements

This work was partly funded by Fondazione Cassa di Risparmio in Bologna through 2018/0348 BEDFLOW and 2019/0228 BEDFLOW PLUS project by the S2S “Slope to Stream” project (CUP: B95F21002540005) awarded within the CNR call PROGETTI@CNR - I AVVISO/2020, and by LASST: evaluating LAndslide Sediment Supply to sTreams and connectivity for sustainable, basin-wide sediment management (CUP: J53D23002600006) awarded within the PRIN 2022 call SP was funded through a PhD scholarship of the Italian Ministry of University (cycle XXXIV). We thank Anna Rita Bernardi, Giuseppe Caputo and Marco Pizziolo of Regione Emilia-Romagna, for sharing their knowledge on landslides in the Northern Apennines. We greatly acknowledge constructive and insightful reviews on an earlier draft conducted by Federica Fiorucci and Roy Sidle. Reviews from three anonymous referees and the Editor, Prof. Yuichi Hayakawa, aided improving the presentation of the main paper's messages.

Appendix A. Supplementary data

Supplementary data to this article can be found online at https://doi.org/10.1016/j.geomorph.2024.109122.

References

Aucelli, P.P.C., Conforti, M., Della Seta, M., Del Monte, M., D'uva, L., Rosskopf, C.M., Vergari, F., 2016. Multi-temporal digital photogrammetric analysis for quantitative assessment of soil erosion rates in the Landola Catchment of the Upper Orcia Valley (Tuscany, Italy). Land Degrad. Dev., 27, 1075–1092. doi:https://doi.org/10.1002/ldr.2324.

Ávila, A., Justino, F., Wilson, A., Bromwich, D., Amorim, M., 2016. Recent precipitation trends, flash floods and landslides in southern Brazil. Environ. Res. Lett. 11, 114029 https://doi.org/10.1088/1748-9326/11/11/114029.

Beguería, S., 2006. Changes in land cover and shallow landslide activity: a case study in the Spanish Pyrenees. Geomorphology 74, 196–206. https://doi.org/10.1016/j.geomorph.2005.07.018.

Bell, R., Petschko, H., Röhrs, M., Dix, A., 2012. Assessment of landslide age, landslide persistence and human impact using airborne laser scanning digital terrain models. Geogr. Ann. Ser. B 94 (1), 135–156. https://doi.org/10.1111/j.1468-0459.2012.00454.x.

Benini, A., De Nardo, M.T., Severi, P., Borsetti, A.M., Negri, A., Vaiani, S.C., 2009. Note Illustrative della Carta Geologica d'Italia alla scala 1:50.000, F. 238 Castel San Pietro Terme. 124 pp., S.EL.CA. Firenze.

Benito, G., Gutiérrez, M., Sancho, C., 1992. Erosion rates in badland areas of the Central Ebro Basin (NE-Spain). Catena 19, 269–286. https://doi.org/10.1016/0341-8162(92)90002-S.

Berti, M., Martina, M.L.V., Franceschini, S., Pignone, S., Simoni, A., Pizziolo, M., 2012. Probabilistic rainfall thresholds for landslide occurrence using a Bayesian approach. J. Geophys. Res. 117, F04006 https://doi.org/10.1029/2012JF002367.

Bertolini, G., Pizziolo, M., 2008. Risk assessment strategies for the reactivation of earth flows in the Northern Apennines (Italy). Eng. Geol. 102 (3–4), 178–192. https://doi.org/10.1016/j.enggeo.2008.03.017.

Bettelli, G., Panini, F., Fioroni, C., Nirta, G., Remitti, F., Vannucchi, P., Carlini, M., 2012. Revisiting the Geology of the “Sillaro Line”, Northern Apennines, Italy. Rend. Online Soc. Geol. It. 22, 14–17.

Bosino, A., Omran, A., Maerker, M., 2019. Identification, characterisation and analysis of the Oltrepo Pavese calanchi in the Northern Apennines (Italy). Geomorphology 340, 53–66. https://doi.org/10.1016/j.geomorph.2019.05.003.

Brardinoni, F., 2001. Identification of Natural and Logging-related Landslides in the Capilano River Basin (Coastal British Columbia): A Comparison Between Remotely Sensed Survey and Field Survey (Master’s thesis). Retrieved from UBC Library. Department of Geography, University of British Columbia, Vancouver, British Columbia.

Brardinoni, F., Church, M., 2004. Representing the landslide magnitude–frequency relation: Capilano River basin, British Columbia. Earth Surf. Process. Landf. 29 (1), 115–124. https://doi.org/10.1002/esp.1029.

Brardinoni, F., Hassan, M.A., Slaymaker, H.O., 2003a. Complex mass wasting response of drainage basins to forest management in coastal British Columbia. Geomorphology 49 (1–2), 109–124. https://doi.org/10.1016/S0169-555X(02)00166-6.

Brardinoni, F., Slaymaker, O., Hassan, A.M., 2003b. Landslide inventory in a rugged forested watershed: a comparison between air-photo and field survey data. Geomorphology 54 (3–4), 179–196. https://doi.org/10.1016/S0169-555X(02)00355-0.

Brardinoni, F., Hassan, M.A., Rollerson, T., Maynard, D., 2009. Colluvial sediment dynamics in 1142 mountain drainage basins. Earth Planet. Sci. Lett. 284 (3–4), 310–319. https://doi.org/10.1016/j.epsl.2009.05.002.

Brardinoni, F., Church, M., Simoni, A., Macconi, P., 2012. Lithologic and glacially conditioned controls on regional debris-flow sediment dynamics. Geology 40 (5), 455–458. https://doi.org/10.1130/G33106.1.

Brunsden, D., 1993. Barriers to geomorphological change. In: Thomas, D.S.G., Allison, R. J. (Eds.), Landscape Sensitivity. John Wiley & Sons, Chichester, pp. 7–12.

Buendia, C., Batalla, R.J, Sabater, S., Palau, A., Marcé, R., 2015. Runoff trends driven by climate and afforestation in a Pyrenean basin. Land Degrad. Dev., 27, 823–838. doi: https://doi.org/10.1002/ldr.2384.

Buma, B., Pawlik, L., 2021. Post-landslide soil and vegetation recovery in a dry, montane system is slow and patchy. Ecosphere 12 (1). https://doi.org/10.1002/ecs2.3346.

Caine, N., 1980. The rainfall intensity-duration control of shallow landslides and debris flows. Soc. Swed. Ann. Geogr. Geogr. Phys. 62, 23–27.

CDS (Climate Data Store), 2021. E-OBS daily gridded meteorological data for Europe from 1950 to present derived from in-situ observations. https://cds.climate.copernicus.eu/cdsapp#!/dataset/insitu-gridded-observations-europe?tab=form (accessed October 2021).

Cevasco, A., Pepe, G., Brandolini, P., 2014. The influences of geological and land use settings on shallow landslides triggered by an intense rainfall event in a coastal terraced environment. Bull. Eng. Geol. Environ. 73, 859–875. https://doi.org/10.1007/s10064-013-0544-x.

Chou, W.C., Lin, W.T., Lin, C.Y., 2009. Vegetation recovery patterns assessment at landslides caused by catastrophic earthquake: a case study in central Taiwan. Environ. Monit. Assess. 152, 245–257. https://doi.org/10.1007/s10661-008-0312-8.

Ciccarese, G., Mulas, M., Alberoni, P.P., Truffelli, G., Corsini, A., 2020. Debris flows rainfall thresholds in the Apennines of Emilia-Romagna (Italy) derived by the analysis of recent severe rainstorms events and regional meteorological data. Geomorphology 358, 107097. https://doi.org/10.1016/j.geomorph.2020.107097.

Ciccarese, G., Mulas, M., Corsini, A., 2021. Combining spatial modelling and regionalization of rainfall thresholds for debris flows hazard mapping in the Emilia-Romagna Apennines (Italy). Landslides 18, 3513–3529. https://doi.org/10.1007/s10346-021-01739-w.

Corine (2023). Corin Land Cover. https://land.copernicus.eu/en/products/corine-land-cover (accessed June 2023).

Coscarelli, R., Aguilar, E., Petrucci, O., Vicente-Serrano, S.M., Zimbo, F., 2021. The potential role of climate indices to explain floods, mass-movement events and wildfires in Southern Italy. Climate 9, 156. https://doi.org/10.3390/cli9110156.

Crosta, G.B., Frattini, P., 2003. Distributed modelling of shallow landslides triggered by intense rainfall. Nat. Hazards Earth Syst. Sci. 3, 81–93. https://doi.org/10.5194/nhess-3-81-2003.

Crozier, M.J., 2010. Deciphering the effect of climate change on landslide activity: a review. Geomorphology 124, 260–267.
Cruden, D.M., Varnes, D.J., 1996. Landslide types and processes. In: Turner, A.K., Schuster, R.L. (Eds.), Landslides, Investigation and Mitigation. Transportation Research Board, Special Report, 247. National Academy Press, pp. 36–75.
Dadson, S.J., Hovius, N., Chen, H., Dade, W.B., Lin, J.C., Hsu, M.L., Lin, C.W., Horng, M. J., Chen, T.C., Milliman, J., Stark, C.P., 2004. Earthquake-triggered increase in sediment delivery from an active mountain belt. Geology 32 (8), 733–736. https://doi.org/10.1130/G20639.1.
Della Seta, M., Del Monte, M., Fredi, P., Lupia Palmieri, E., 2009. Space–time variability of denudation rates at the catchment and hillslope scales on the Tyrrhenian side of Central Italy. Geomorphology 107 (3–4), 161–177. https://doi.org/10.1016/j.geomorph.2008.12.004.
Gallart, F., Solé, A., Puigdefábregas, J., Lázaro, R., 2002. Badland systems in the Mediterranean. In: Bull, J.L., Kirkby, M.J. (Eds.), Dryland Rivers: Hydrology and Geomorphology of Semi-arid Channels. John Wiley & Sons Ltd., Chichester, pp. 299–326.
García-Ruiz, J.M., Lasanta, T., Ruiz-Flaño, P., Ortigosa, L., White, S., González, C., Martí, C., 1996. Land-use changes and sustainable development in mountain areas: a case study in the Spanish Pyrenees. Landsc. Ecol. 11 (5), 267–277. https://doi.org/10.1007/BF02059854.
Glade, T., 2003. Landslide occurrence as a response to land use change: a review of evidence from New Zealand. Catena 51 (3–4), 297–314. https://doi.org/10.1016/S0341-8162(02)00170-4.
Guzzetti, F., Cardinali, M., Reichenbach, P., 1996. The influence of structural setting and lithology on landslide type and pattern. Environ. Eng. Geosci. 2-4, 531–555. https://doi.org/10.2113/gseegeosci.II.4.531.
Guzzetti, F., Peruccacci, S., Rossi, M., Stark, C.P., 2008. The rainfall intensity-duration control of shallow landslides and debris flows: an update. Landslides 5, 3–17. https://doi.org/10.1007/s10346-007-0112-1.
Guzzetti, F., Mondini, A.C., Cardinali, M., Fiorucci, F., Santangelo, M., Chang, K., 2012. Landslide inventory maps: new tools for an old problem. Earth Sci. Rev. 112 (1–2), 42–66. https://doi.org/10.1016/j.earscirev.2012.02.001.
Hoelzle, M., Haeberli, W., Dischl, M., Peschke, W., 2003. Secular glacier mass balances derived from cumulative glacier length changes. Glob. Planet. Chang. 36, 295–306. https://doi.org/10.1016/S0921-8181(02)00223-0.
Hussin, H.Y., Zumpano, V., Reichenbach, P., Sterlacchini, S., Micu, M., van Westen, C., Bălteanu, D., 2016. Different landslide sampling strategies in a grid-based bi-variate statistical susceptibility model. Geomorphology 253, 508–523. https://doi.org/10.1016/j.geomorph.2015.10.030.
IGM (2023). Istituto Geografico Militare – Foto Aeree. https://www.igmi.org/it/descrizione-prodotti/aerial-photography (accessed June 2023).
Imaizumi, F., Sidle, R.C., Kamei, R., 2008. Effects of forest harvesting on the occurrence of landslides and debris flows in steep terrain of central Japan. Earth Surf. Process. Landf. 33 (827–840) https://doi.org/10.1002/esp.1574.
Jakob, M., 2000. The impacts of logging on landslide activity at Clayoquot Sound, British Columbia. Catena 38 (4), 279–300. https://doi.org/10.1016/S0341-8162(99)00078-8.
Kaiserlich-Königliches Militär-Geographisches Institut, 1851. Topographische Karte Des Kirchenstaates Und Des Grossherzogthumes Toscana: nach astronomisch trigonometrischen Vermessungen bearbeitet und auf Stein gestochen zu Wien, Maßstab 1:86400, Blatt E8.
La Licata, M., Bosino, A., Bettoni, M., Maerker, M., 2023. Assessing landscape features and geomorphic processes influencing sediment dynamics in a geomorphologically highly active Mediterranean agroecosystem: the upper Val d'Arda case study (Northern Apennines, Italy). Geomorphology 433, 108724. https://doi.org/10.1016/j.geomorph.2023.108724.
Liébault, F., Piégay, H., 2002. Causes of 20th century channel narrowing in mountain and piedmont rivers of southeastern France. Earth Surf. Process. Landf. 27, 425–444. https://doi.org/10.1002/esp.328.
Llena, M., Vericat, D., Smith, M.W., Wheaton, J.M., 2020. Geomorphic process signatures reshaping sub-humid Mediterranean Badlands: 1. Methodological development based on high-resolution topography. Earth Surf. Process. Landf. 45 (5), 1335–1346. https://doi.org/10.1002/esp.4821.
Llena, M., Simonelli, T., Brardinoni, F., 2024. Inherited anthropogenic disturbance and decadal sediment dynamics in a mountain fluvial system: the case of the Marecchia River canyon, Northern Apennines. Geol. Soc. Am. Bull. 136 (1–2), 741–764. https://doi.org/10.1130/B36720.1.
Luna, L.V., Korup, O., 2022. Seasonal landslide activity lags annual precipitation pattern in the Pacific Northwest. Geophys. Res. Lett. 49 (18), e2022GL098506.
Mathys, N., Brochot, S., Meunier, M., Richard, D., 2003. Erosion quantification in the small marly experimental catchments of Draix (Alpes de Haute Provence, France). Calibration of the ETC rainfall–runoff–erosion model. Catena 50 (2–4), 527–548. https://doi.org/10.1016/S0341-8162(02)00122-4.
McEachran, Z.P., Karwan, D.L., Slesak, R.A., 2020. Direct and indirect effects of forest harvesting on sediment yield in forested watersheds of the United States. J. Am. Water Resour. Assoc. 57 (1), 1–31. https://doi.org/10.1111/1752-1688.12895.
Mondini, A.C., Guzzetti, F., Reichenbach, P., Rossi, M., Cardinali, M., Ardizzone, F., 2011. Semi-automatic recognition and mapping of rainfall induced shallow landslides using optical satellite images. Remote Sens. Environ. 115 (7), 1743–1757. https://doi.org/10.1016/j.rse.2011.03.006.
Mondini, A.C., Guzzetti, F., Chang, K.T., Monserrat, O., Martha, T.R., Manconi, A., 2021. Landslide failures detection and mapping using Synthetic Aperture Radar: past, present and future. Earth Sci. Rev. 216, 103574 https://doi.org/10.1016/j.earscirev.2021.103574.
Mysiak, J., Torresan, S., Bosello, F., Mistry, M., Amadio, M., Marzi, S., Furlan, E., Sperotto, A., 2018. Climate risk index for Italy. Philos. Trans. A Math. Phys. Eng. Sci. 376, 2017030 https://doi.org/10.1098/rsta.2017.0305.
Nadal-Romero, E., Lana-Renault, N., Serrano-Muela, P., Regüés, D., Alvera, B., García-Ruiz, J.M., 2012. Sediment balance in four catchments with different land cover in the Central Spanish Pyrenees. Z. Geomorphol. 56 (Suppl. 3), 147–168. https://doi.org/10.1127/0372-8854/2012/S-00109.
Nadal-Romero, E., Rodríguez-Caballero, E., Chamizo, S., Juez, C., Cantón, Y., García-Ruíz, J.M., 2021. Mediterranean badlands: their driving processes and climate change futures. Earth Surf. Process. Landf. 1–15. https://doi.org/10.1002/esp.5088.
Patzelt, G., 1985. The period of glacier advances in the Alps, 1965 to 1980. Z. Gletscherk. Glazialgeol. 21, 403–407.
Pavanelli, D., Cavazza, C., Lavrnic, S., Toscano, A., 2019. The long-term effects of land use and climate changes on the hydro-morphology of the Reno River Catchment (Northern Italy). Water 11, 1831. https://doi.org/10.3390/w11091831.
Persichillo, M.G., Bordoni, M., Meisina, C., 2017. The role of land use changes in the distribution of shallow landslides. Sci. Total Environ. 574, 924–937. https://doi.org/10.1016/j.scitotenv.2016.09.125.
Piccarreta, M., Capolongo, D., Boenzi, F., Bentivenga, M., 2006. Implications of decadal changes in precipitation and land use policy to soil erosion in Basilicata, Italy. Catena 65, 138–151. https://doi.org/10.1016/j.catena.2005.11.005.
Pisano, L., Zumpano, V., Malek, Ž., Rosskopf, C.M., Parise, M., 2017. Variations in the susceptibility to landslides, as a consequence of land cover changes: a look to the past, and another towards the future. Sci. Total Environ. 601–602, 1147–1159. https://doi.org/10.1016/j.scitotenv.2017.05.231.
Pittau, S., Pizziolo, M., Rossi, M., Brardinoni, F., 2021. A multi-temporal mapping approach for improving the temporal and spatial characterization of landslide activity in clay-rich terrain. Rend. Online Soc. Geol. It. 54, 17–31. https://doi.org/10.3301/ROL.2021.06.
Preciso, E., Salemi, E., Billi, P., 2012. Land use changes, torrent control works and sediment mining: effects on channel morphology and sediment flux, case study of the Reno River (Northern Italy). Hydrol. Process. 26 (8), 1134–1148. https://doi.org/10.1002/hyp.8202.
Pyles, M.R., Froehlich, H.A., 1987. Discussion of "Rates of landsliding as impacted by timber management activities in northwestern California," by M. Wolfe and J. Williams. Bull. Assoc. Eng. Geol. 24, 425–431.
Ranga, V., Poesen, J., Van Rompaey, A., Mohapatra, S.N., Pani, P., 2016. Detection and analysis of badlands dynamics in the Chambal River Valley (India), during the last 40 (1971–2010) years. Environ. Earth Sci. 75, 1–12. https://doi.org/10.1007/s12665-015-5017-z.
Regione Emilia-Romagna, 2023. Database uso del suolo della Regione Emilia-Romagna. https://geoportale.regione.emilia-romagna.it/approfondimenti/database-uso-del-suolo (accessed June 2023).
Regione Toscana, 2023. Uso e Copertura del Suolo della Regione Toscana. https://dati.toscana.it/dataset/ucs (accessed June 2023).
Regüés, D., Pardini, G., Gallart, F., 1995. Regolith behaviour and physical weathering of clayey mudrock as dependent on seasonal weather conditions in a badland area at Vallcebre, Eastern Pyrenees. Catena 25, 199–212. https://doi.org/10.1016/0341-8162(95)00010-P.
Reid, L.M., Dunne, T., 1996. Rapid Evaluation of Sediment Budgets. Catena Verlag, Reiskirchen, Germany.
Rood, K.M., 1984. An Aerial Photograph Inventory of the Frequency and Yield of Mass Wasting on the Queen Charlotte Islands, British Columbia. Land Management Report. (Vol. 34). BC Ministry of Forests, Victoria, Canada.
Rossi, M., Witt, A., Guzzetti, F., Malamud, B.D., Peruccacci, S., 2010. Analysis of historical landslide time series in the Emilia-Romagna region, northern Italy. Earth Surf. Process. Landf. 35 (10), 1123–1137. https://doi.org/10.1002/esp.1858.
Saito, H., Uchiyama, S., Teshirogi, K., 2022. Rapid vegetation recovery at landslide scars detected by multitemporal high-resolution satellite imagery at Aso volcano, Japan. Geomorphology 398. https://doi.org/10.1016/j.geomorph.2021.107989.
Scorpio, V., Piégay, H., 2021. Is afforestation a driver of change in Italian rivers within the Anthropocene era? Catena 198, 105031. https://doi.org/10.1016/j.catena.2020.10503.
Scotti, R., Brardinoni, F., Crosta, G.B., 2014. Post-LIA glacier changes along a latitudinal transect in the Central Italian Alps. Cryosphere 8 (6), 2235–2252. https://doi.org/10.5194/tc-8-2235-2014.
Seixas, G.B., Veldhuisen, C.N., 2023. Forest management history influences eight decades of shallow landsliding in the northwest Cascade Mountains, USA. Earth Surf. Process. Landf. 48, 2716–2736. https://doi.org/10.1002/esp.5656.
Sidle, R.C., Bogaard, T.A., 2016. Dynamic earth system and ecological controls of rainfall-initiated landslides. Earth Sci. Rev. 159, 275–291. https://doi.org/10.1016/j.earscirev.2016.05.013.
Sidle, R.C., Ochiai, H., 2006. Landslides Processes, Prediction, and Land Use. Water Resources Monograph Series, 18. American Geophysical Union, Washington DC, USA.
Simoni, A., Ponza, A., Picotti, V., Berti, M., Dinelli, E., 2013. Earthflow sediment production and Holocene sediment record in a large Apennine catchment. Geomorphology 188, 42–53. https://doi.org/10.1016/j.geomorph.2012.12.006.
Slaymaker, O., Spencer, T., Embleton-Hamann, C., 2009. Geomorphology and Global Environmental Change. Cambridge University Press.
Smith, R.B., Commandeur, P.R., Ryan, M.W., 1986. Soils, vegetation, and forest growth on landslides and surrounding logged and old-growth areas on the Queen Charlotte Islands. In: Land Management Report, vol. 41. BC Ministry of Forests, Victoria, Canada.
Stark, C.P., Hovius, N., 2001. The characterization of landslide size distributions. Geophys. Res. Lett. 28, 1091–1094. https://doi.org/10.1029/2000GL008527.

Torri, D., Santi, E., Marignani, M., Rossi, M., Borselli, L., Maccherini, S., 2013. The recurring cycles of biancana badlands: erosion, vegetation and human impact. Catena 106, 22–30. https://doi.org/10.1016/j.catena.2012.07.001.

Torri, D., Rossi, M., Brogi, F., Marignani, M., Bacaro, G., Santi, E., Tordoni, E., Amici, V., Maccherini, S., 2018. Badlands and the dynamics of human history, land use, and vegetation through centuries. In: Nadal-Romero, E., Martínez- Murillo, J.F., Kuhn, N. J. (Eds.), Badland Dynamics in the Context of Global Change. Elsevier, Amsterdam. https://doi.org/10.1016/B978-0-12-813054-4.00004-6.

Turner, T.R., Duke, S.D., Fransen, B.R., Reiter, M.L., Kroll, A.J., Ward, J.W., Bach, J.L., Justice, T.E., Bilby, R.E., 2010. Landslide densities associated with rainfall, stand age, and topography on forested landscapes, southwestern Washington, USA. For. Ecol. Manag. 259 (12), 2233–2247. https://doi.org/10.1016/j.foreco.2010.01.051.

Vergani, C., Giadrossich, F., Buckley, P., Conedera, M., Pividori, M., Salbitano, F., Rauchg, H.S., Lovreglio, R., Schwarz, M., 2017. Root reinforcement dynamics of European coppice woodlands and their effect on shallow landslides: a review. Earth Sci. Rev. 167, 88–102. https://doi.org/10.1016/j.earscirev.2017.02.002.

Vergari, F., Della Seta, M., Del Monte, M., Barbieri, M., 2013. Badlands denudation "hot spots": the role of parent material properties on geomorphic processes in 20-years monitored sites of Southern Tuscany (Italy). Catena 106, 31–41. https://doi.org/10.1016/j.catena.2012.02.007.

Vergari, F., Troiani, F., Faulkner, H., Del Monte, M., Della Seta, M., Ciccacci, S., Fredi, P., 2019. The use of the slope–area function to analyse process domains in complex badland landscapes. Earth Surf. Process. Landf. 44, 273–286. https://doi.org/10.1002/esp.4496.

Vericat, D., Smith, M.W., Brasington, J., 2014. Patterns of topographic change in sub-humid badlands determined by high resolution multi-temporal topographic surveys. Catena 120, 164–176. https://doi.org/10.1016/j.catena.2014.04.012.

Witt, A., Malamud, B.D., 2013. Quantification of long-range persistence in geophysical time series: conventional and benchmark-based improvement techniques. Surv. Geophys. 34, 541–651. https://doi.org/10.1007/s10712-012-9217-8.

Witt, A., Malamud, B.D., Rossi, M., Guzzetti, F., Peruccacci, S., 2010. Temporal correlations and clustering of landslides. Earth Surf. Process. Landf. 35 (10), 1138–1156. https://doi.org/10.1002/esp.1998.

Yair, A., Lavee, H., Bryan, R.B., Adar, E., 1980. Runoff and erosion processes and rates in the Zin Valley badlands, Northern Negev, Israel. Earth Surf. Process. 5, 205–225. https://doi.org/10.1002/esp.3760050301.

Zattin, M., Picotti, V., Zuffa, G.G., 2002. Fission-track reconstruction of the front of the Northen Apennine thrust wedge and overlying Ligurian Unit. Am. J. Sci. 302 (4), 346–379. https://doi.org/10.2475/ajs.302.4.346.

Zeng, Z., Estes, L., Ziegler, A.D., Chen, A., Searchinger, T., Hua, F., Guan, K., Jintrawet, A., Wood, E.F., 2018. Highland cropland expansion and forest loss in Southeast Asia in the twenty-first century. Nat. Geosci. 11, 556–562. https://doi.org/10.1038/s41561-018-0166-9.

Zêzere, J.L., Vaz, T., Pereira, S., Oliveira, S.C., Marques, R., Garcia, R.A., 2015. Rainfall thresholds for landslide activity in Portugal: a state of the art. Environ. Earth Sci. 73, 2917–2936.